BB-SPEEDset: A Validated Dataset of Broadband Near-Source Earthquake Ground Motions from 3D Physics-Based Numerical Simulations

Roberto Paolucci[1], Chiara Smerzini*[1], and Manuela Vanini[1]

ABSTRACT

This article introduces a strong-motion dataset of near-source broadband earthquake ground motions from 3D physics-based numerical simulations—named BB-SPEEDset—obtained by the code SPEED (SPectral Elements in Elastodynamics with Discontinuous Galerkin)—developed at Politecnico di Milano, Italy. Taking advantage of the earthquake ground-motion scenarios produced so far by SPEED, in most cases validated against earthquake recordings, the main objective of this work is to construct and validate a dataset of simulated broadband waveforms to be used as a support for characterization and modeling of near-source earthquake ground motions. To pursue this objective, the following steps were necessary, namely: (1) the implementation of an effective workflow suitable to process in an homogeneous format various SPEED simulations; (2) the generation of broadband time histories using a technique based on artificial neural networks, trained on strong-motion records; (3) the creation of a flat file collecting, for each simulated scenario, the most relevant metadata (fault rupture scenario, site response proxies, source-to-site distances) as well as a comprehensive set of ground-motion intensity measures of the processed broadband waveforms (peak ground acceleration, velocity and displacement, spectral ordinates, duration, pulse period, etc.). Finally, a comprehensive set of consistency checks is made to verify the absence of any systematic bias in the trend of the BB-SPEEDset results with respect to the NEar-Source Strong-motion (NESS) version 2.0 near-source recorded ground-motion dataset. Indeed, the main features of near-source ground motion in BB-SPEEDset, ranging from the statistical distributions of peak and integral measures both at short and long periods, the ground-motion attenuation with distance, to the features of impulsive ground motions and directionality effects, are in substantial agreement with those from NESS.

KEY POINTS

- A dataset of broadband near-source ground motions from 3D physics-based numerical simulations is created.
- The features of BB-SPEEDset are consistent with the NEar-Source Strong-motion dataset (NESS).
- BB-SPEEDset may serve as a support for an improved characterization of near-source ground motions.

INTRODUCTION

It is well known that the characterization of earthquake ground motion in the near-source region is made difficult by the paucity of records that, in spite of their evergrowing number, cannot reliably describe yet neither the median values nor their variability, in the variety of source and site conditions typically present in the vicinity of the seismogenic fault.

As in most fields of science, when the laboratory investigations are either limited or prevented owing to the size of the prototype and to the difficulties to reproduce the in-field conditions, analytical and numerical modeling may be an alternative to complement in an ideal laboratory the information that is difficult to capture from nature.

In this perspective, the so-called physics-based numerical simulations (PBS) of earthquake ground motion aim at complementing the recorded data by providing simulated results in the source and site configurations that may resemble as closely as possible the real ones. In some cases, the role of PBS has been extended to provide realistic seismic scenarios of earthquake ground motions suitable to improve the approaches for

1. Department of Civil and Environmental Engineering, Politecnico di Milano, Milan, Italy, https://orcid.org/0000-0002-5856-9916 (RP); https://orcid.org/0000-0003-4357-6934 (CS); https://orcid.org/0000-0001-8164-2475 (MV)

*Corresponding author: chiara.smerzini@polimi.it

Cite this article as Paolucci, R., C. Smerzini, and M. Vanini (2021). BB-SPEEDset: A Validated Dataset of Broadband Near-Source Earthquake Ground Motions from 3D Physics-Based Numerical Simulations, *Bull. Seismol. Soc. Am.* **XX**, 1–19, doi: 10.1785/0120210089

seismic hazard and risk analysis (see e.g., Graves *et al.*, 2011; Maeda *et al.*, 2016; Bradley *et al.*, 2017, 2020; Smerzini and Pitilakis, 2018; Stupazzini *et al.*, 2021) and to provide input for seismic structural analyses (Galasso *et al.*, 2013; Baker *et al.*, 2021; Fayaz *et al.*, 2021).

With this objective, several research groups worldwide (see e.g., amongst others, Graves and Pitarka, 2010, 2015; Irikura and Miyake, 2011; Komatitsch *et al.*, 2013; Mazzieri *et al.*, 2013; Isbiliroglu *et al.*, 2015; Lu *et al.*, 2018; Paolucci *et al.*, 2018; McCallen, Petersson, *et al.*, 2020; McCallen, Petrone, *et al.*, 2020) have continuously contributed in the recent years to the development of numerical tools that may become more and more suitable to produce, with a reasonable computational effort, realistic earthquake ground motions that may reliably complement the recorded ones in the near-source region and eventually be coupled with engineering models for nonlinear structural response.

Combining the computational burden with the difficulty to accurately reproduce details of the fault geometry, of the seismic slip distribution, and of the complex geology (typically 3D) of the area of interest, that may extend by tens of kilometers, PBS are generally considered to be bounded within frequency limits hardly beyond about 2–3 Hz, although some successful examples of PBS extending up to 8–10 Hz in the presence of very detailed knowledge of local site conditions are also present, such as for the simulation of induced seismicity in the Groningen (the Netherlands) area (Paolucci *et al.*, 2021).

Some cross-verification activities of numerical tools for PBS were undertaken in the recent past (Bielak *et al.*, 2010; Chaljub *et al.*, 2010; Maufroy *et al.*, 2015) that were seminal steps for the different research groups to solve the major issues arising when the numerical codes are applied to very complex configurations. However, relatively little effort was devoted up to now to comprehensive validations of PBS against strong-motion records, especially in the near-source region (Taborda and Bielak, 2013, 2014; Paolucci *et al.*, 2015, 2021; Imperatori and Gallovič, 2017; Gatti *et al.*, 2018; Pitarka *et al.*, 2020). For this reason, a blind prediction experiment was set up in the framework of the 6th International Symposium on the Effects of Surface Geology on Seismic Motion (ESG6), jointly supported by the International Association of Seismology and Physics of the Earth's Interior (IASPEI) and the International Association of Earthquake Engineering (IAEE), with the objective to reproduce earthquake ground motions during the Kumamoto, Japan, seismic sequence of 2016, with a moment magnitude M_w 7 mainshock.

With a long-lasting expertise gained (1) in the development of the open-source numerical code SPEED based on spectral elements (Mazzieri *et al.*, 2013), (2) in the advancement of techniques to enrich at high frequencies the PBS results (Paolucci *et al.*, 2018), (3) in the validation of PBS results against near-source ground motions recorded from different earthquakes in Italy and worldwide, and in the application to several scenario case studies (see overview in Table 1), we have collected a large subset of our simulated results with a uniform processing procedure that will be illustrated in the sequel. In this way, we have constructed the BB-SPEEDset version 1.0 (v.1.0)—a dataset of broadband near-source ground motions aiming at providing a complementary tool for the characterization of earthquake ground motions, in terms of their dependency on magnitude, distance, and site conditions, such as the most common empirical ground-motion models (GMMs), with a complete and well-constrained description in terms of seismic source and site conditions. In addition, this dataset may also provide the basis to properly analyze the spatial variability of ground motion, with potential important implications to validate and improve the existing models for spatial correlation (e.g., Infantino, Smerzini, and Lin, 2021; Schiappapietra and Smerzini, 2021) and spatial coherency that currently suffer from the lack of records from sufficiently densely spaced arrays of seismic stations (e.g., Smerzini, 2018).

As introduced by D'Amico *et al.* (2017), the main advantage of a broadband ground-motion dataset based on PBS is that all input source data are clearly identified, as well as the site conditions of recording stations, and ground-shaking scenarios of the simulated earthquakes can easily be constructed. On the other side, it is difficult to prove that the available waveforms are not biased with respect to records, in terms of the different parameters of ground motion that are relevant for engineering applications, typically because of the limited detail of the input data of PBS in terms of seismic source and geological layering, and because of the computational limits of the numerical simulations.

To overcome such limitations, the novelty of this article is to provide a comprehensive comparison of the BB-SPEEDset statistical distributions with those obtained by the NEar-Source Strong-motion dataset NESS (v.2.0)—a dataset of worldwide recorded near-source ground motions addressed in this special issue by Sgobba *et al.* (2021), updated after Pacor *et al.* (2018). Although the origin of the two datasets is completely different, BB-SPEEDset being based on relatively few earthquake scenarios, each with a large sample of simulated accelerograms, whereas NESS is based on a large number of real earthquakes, each with relatively few records, such comparison is a crucial step to assess whether a bias exists between the trend of simulated results in the BB-SPEEDset with respect to those of NESS. The absence of systematic differences will strongly support the effectiveness of the procedure to produce broadband waveforms from the PBS as well as the potential use of the BB-SPEEDset to improve the available tools for the prediction of near-source earthquake ground motion and to provide input motions for earthquake engineering analyses.

This article is organized as follows. After an introduction of the workflow for postprocessing PBS results and for generating broadband waveforms by taking advantage of artificial neural networks (ANNs), the BB-SPEEDset is introduced with its current features, in terms of distribution of simulated waveforms according to magnitude, distance, and site conditions. Subsequently, a comprehensive comparison of the

TABLE 1
Numerical Simulations Performed by the Code SPEED

Case Study	Fault (SoF)	M_w	Model Size (km^3)	$V_{S,min}$ (m/s)	f_{max} (Hz)	Event for Validation	References	Included in BB-SPEEDset
Grenoble, France	Belledonne (SS)	6.0	41 × 50 × 8	300	3	Benchmark	Stupazzini *et al.* (2009)	Not included yet
Gubbio plain, central Italy	Colfiorito (NF)	6.0	85 × 62 × 10	250	3	1997/09/26	Smerzini *et al.* (2011)	Not included yet
Tagliamento plain, northern Italy	Gemona Faults (TF)	6.1	57 × 53 × 12	300	2.5	1976/09/15	Smerzini (2010)	Not included yet
L'Aquila, central Italy	Paganica (NF)	6.2	58 × 58 × 20	300	2.0	2009/04/06	Evangelista *et al.* (2017)	2009 6.2 Aquila
Sulmona, central Italy	Mt. Morrone (NF)	6.0 6.5	49 × 42 × 13	500	2.5	Ideal scenarios	Villani *et al.* (2014)	6.0 SulmonaS03, 6.0 SulmonaS04 6.5 SulmonaS03, 6.5 SulmonaS05
Christchurch, New Zealand	Lyttelton (TF)	6.3	60 × 60 × 20	300	2.0	2011/02/22	Guidotti *et al.* (2011)	Not included yet
Po Plain, northern Italy	Mirandola (TF)	6.0	74 × 51 × 20	300	1.5	2012/05/29	Paolucci *et al.* (2015)	2012 6.0 Emilia
Marsica, central Italy	Fucino (NF)	6.7	56 × 46 × 20	100	2.0	1915/01/13	Paolucci *et al.* (2016)	1915 6.7 Marsica
Thessaloniki, northern Greece	Gerakarou (NF)	6.5	82 × 64 × 31	300	1.5	1978/06/20	Smerzini *et al.* (2017)	1978 6.5 Salonicco
	Anthemountas (NF)	7.0				Ideal scenario	Smerzini *et al.* (2018)	7.0 SaloniccoS01
Norcia, central Italy	Mt. Vettore–Mt. Bove (NF)	6.5 5.8 5.5	50 × 40 × 21	280	1.5	2016/10/30 Ideal scenarios	Özcebe *et al.* (2019)	2016 6.5 Norcia 5.8 NorciaS01 5.5 NorciaS01
Wellington, New Zealand	Wellington–Hutt (SS)	6.0–7.0	80 × 50 × 45	300	2.0	Ideal scenarios	Paolucci *et al.* (2014)	Not included yet
Santiago, Chile	San Ramon (TF)	6.0, 6.5, 7.0	97 × 77 × 19	400	2.0	2010/04/01	Pilz *et al.* (2011)	Not included yet
Istanbul, Turkey	North Anatolian fault–Marmara Sea (SS)	5.7	165 × 100 × 30	250	1.5	2019/09/26	Infantino *et al.* (2021)	Not included yet
		7.0				Ideal scenarios	Stupazzini *et al.* (2021)	7.0 IstanbulS16, 7.0 IstanbulS20, 7.0 IstanbulS23
		7.2				Ideal scenarios		7.2 IstanbulS05, 7.2 IstanbulS09, 7.2 IstanbulS19
		7.4				Ideal scenarios		7.4 IstanbulS02, 7.4 IstanbulS12, 7.4 IstanbulS20
Beijing, China	Shunyi–Qianmen–Liangxiang (TF)	6.5, 6.9, 7.3	70 × 70 × 30	200	1.5	Ideal scenarios	Antonietti *et al.* (2020)	Not included yet
Groningen, the Netherlands	NF	3.4	20 × 20 × 5	150	10	2018/01/08	Paolucci *et al.* (2021)	Not included yet
Kumamoto, Japan	Hinagu–Futagawa–Aso Caldera (SS)	7.0	53 × 46 × 22	500	1.5	2016/04/15 (16:25 UTC)	Sangaraju *et al.* (2021)	2016 7.0 Kumamoto
	Hinagu–Futagawa (SS)	6.1				2016/04/14 (12:26 UTC)		Not included yet
	Aso Caldera (SS)	5.5				2016/04/15 (18:03 UTC)		Not included yet

The scenarios included in BB-SPEEDset are specified in the last column. f_{max}, maximum frequency of the numerical model; M_w, moment magnitude; NF, normal fault; SoF, style of faulting; SS, strike slip; TF, thrust fault, and $V_{S,min}$, minimum shear-wave velocity.

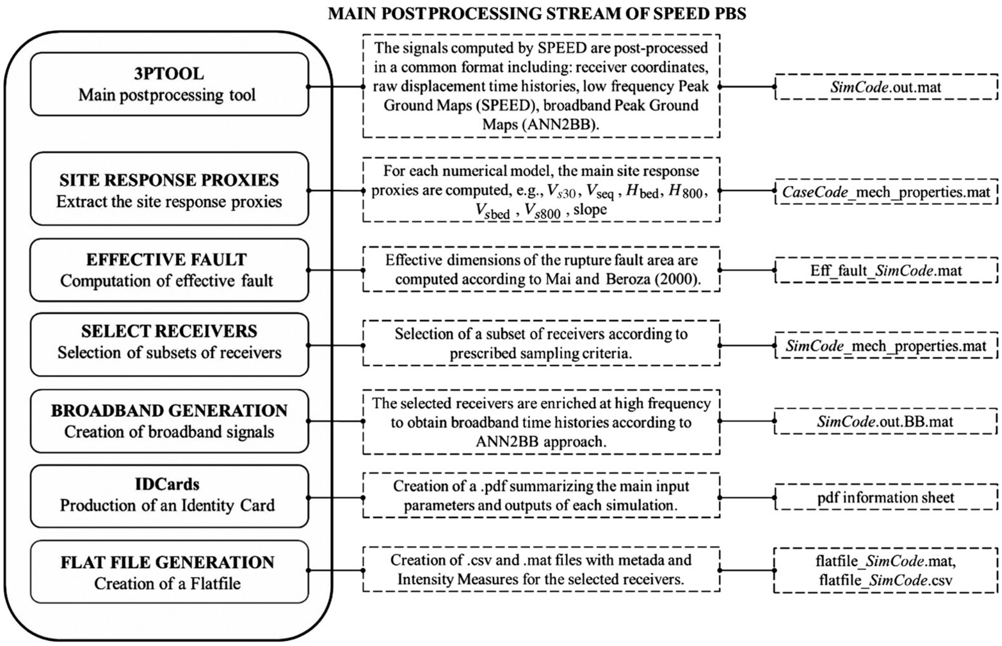

Figure 1. Workflow for postprocessing of SPEED results and creation of the corresponding flat file for BB-SPEEDset. Postprocessing codes are available to SPEED users on demand.

BB-SPEEDset trends with respect to those of the NESS dataset is presented, involving the statistical distribution of various intensity measures (IMs), their attenuation with distance, and the main features of near-source ground motion such as directionality, vertical components, and impulsive motions. Finally, an example of a query by earthquake scenario from the BB-SEEDset is introduced with reference to the 2009 L'Aquila earthquake, where one of the main advantages of a dataset based on PBS can be appreciated, in terms of generation of ground-motion maps of a selected earthquake scenario.

WORKFLOW FOR POSTPROCESSING OF SPEED RESULTS

A fundamental step for the construction of a database of PBS results is the definition of an optimized workflow for postprocessing of results of SPEED simulations in a uniform and repeatable format. To this end, the SPEED kernel is supplemented by a set of MATLAB routine packages (available to SPEED users on demand) that allow to postprocess the raw waveforms computed by SPEED (typically, displacement time histories at receiver points), and generate outputs and metadata in a standard format. Note that, for the earthquake scenarios included in BB-SPEEDset, kinematic rupture models were introduced, consisting of heterogeneous slip functions across the fault. Although for real earthquakes (validations in Table 1), the kinematic source parameters were calibrated based on the available seismic source inversions studies, for scenario earthquakes the kinematic rupture generators proposed by Herrero and Bernard (1994) and Schmedes *et al.* (2012) are adopted. The generation of these fault-slip distributions is handled by means of specific MATLAB routines, implemented in the preprocessing tools of SPEED.

An overview of the postprocessing workflow is given in Figure 1, and it is organized in the following steps:

- 3PTOOL: The code extracts and organizes the raw SPEED seismograms in a common format (output file: Matlab .mat file), including receiver coordinates, displacement time histories (unfiltered), low frequency (directly from SPEED), and broadband (from Artificial Neural Network to BroadBand ground motions (ANN2BB); see Broadband Generation section) peak ground motion maps.
- SITE RESPONSE PROXIES: The routine computes from the velocity model the most relevant site response proxies, namely: H_{bed}—depth of the alluvial-bedrock interface included in the simulation model, H_{800}—depth at which the shear-wave velocity V_S is equal or higher than 800 m/s, V_{S30}—time averaged shear-wave velocity from the surface to a depth of 30 m, V_{Seq}—time averaged shear-wave velocity from the surface to H_{800} (if $H_{800} \le 30$ m; if $H_{800} > 30$ m, then $H_{800} = 30$ m), [see definition in the Italian Building Code (Norme Tecniche per le Costruzioni [NTC], 2018)], V_{Sbed}–time averaged shear-wave velocity from the surface to H_{bed}, V_{S800}—time averaged shear-wave velocity from the surface to H_{800}; topography slope.
- EFFECTIVE FAULT: The code calculates the effective dimensions of the rupture fault area according to the procedure originally proposed by Mai and Beroza (2000), and extended by Thingbaijam and Mai (2016) (see Figure 2). This step is particularly relevant to define metadata with unbiased source dimensions, as the fault implemented in the numerical grid (typically, the fault associated with a maximum magnitude to be simulated) may be different from the coseismic rupture area associated with a given earthquake scenario. Effective source dimensions are based on the definition of autocorrelation width (Bracewell, 1986) of slip distributions, calculated in along-strike and down-dip directions. These slip functions are computed summing up the slip in columns (or rows) on the rectangular rupture plane. An iterative, trimming process determines the largest dimensions that fit the autocorrelation width, according to the

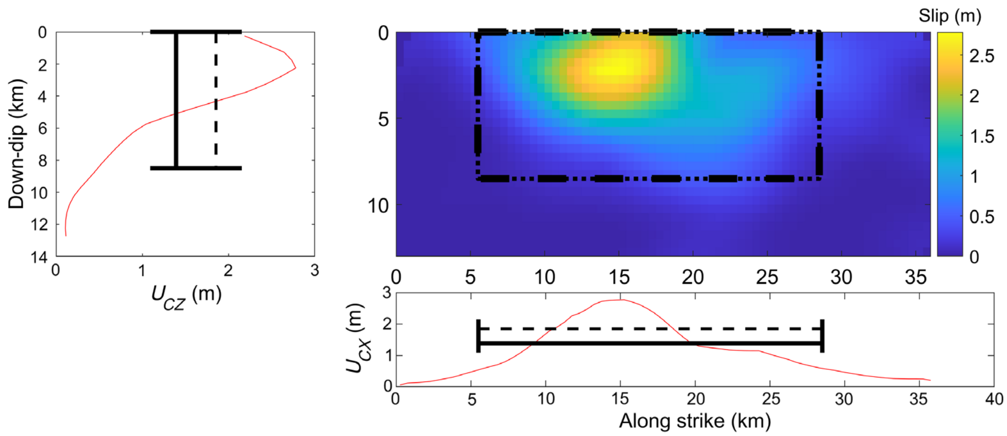

Figure 2. Computation of the effective fault dimensions according to the procedure proposed by Mai and Beroza (2000) and extended by Thingbaijam and Mai (2016). The color version of this figure is available only in the electronic edition.

subfault size. The dependence of these effective measures on magnitude through scaling relationships has been verified (using e.g., Wells and Coppersmith, 1994 or Leonard, 2010).

- SELECT RECEIVERS: The code extracts subsets of receiver points according to prescribed sampling techniques. Because the simulated seismograms are generally obtained at tens of thousands of receivers, the computation of broadband time histories and of all corresponding IMs is limited to a subset of receivers to minimize the computational cost. In our processing for the BB-SPEEDset, the receiver selection was defined to achieve a higher density of receivers at lower distances from the source.
- BROADBAND GENERATION: At the selected receivers, the SPEED signals (typically reliable up to about 1.5–2 Hz; see Table 1) are enriched at high frequencies using a technique based on ANN trained on strong ground motion recordings (referred to as ANN2BB).
- SPEED IDCards: The routine produces an informative sheet (.pdf) summarizing the main features of the numerical model (e.g., mesh, wave velocity model), of the simulated fault rupture scenario (e.g,. fault-slip distribution, rise time, rupture times), and of a selection of outputs (e.g., ground-shaking maps).
- FLAT FILE GENERATION: A flat file is created in a format consistent with the one adopted in up-to-date strong-motion databases (e.g., NESS) and populated with an exhaustive list of metadata (regarding the source, source-to-site distances, site response proxies, postprocessing, etc.) and ground-motion IMs.

BROADBAND GENERATION

As well known, the accuracy of the PBS is limited to the long-period range $T \geq T^*$, with T^* being typically in the range of 0.5–1 s (see maximum frequency in Table 1), mainly due to the lack of knowledge about the Earth crust and earthquake rupture process at short wavelength and partially due to the computational cost of large and fine grids. For this reason, the core of the postprocessing workflow is the generation of broadband waveforms, in which the low-frequency simulated waveforms are enriched in the high-frequency range to produce time histories with a realistically broad frequency content. This is an essential step to treat the simulated waveforms in the same way as recordings, and, therefore, make them usable in earthquake engineering applications.

To this end, the ANN2BB approach (Paolucci *et al.*, 2018), based on ANNs trained on strong ground motion recordings, is adopted. In this work, the ANN2BB technique has been enhanced with respect to the original version published in 2018 to make it suitable for massive postprocessing of larger datasets in a semiautomated fashion and to improve the quality of generated waveforms.

Referring to Paolucci *et al.* (2018) for further details, the ANN2BB procedure is based on four main steps, as sketched in Figure 3:

1. An ANN, consisting of two-layer feed-forward neural network with 30 hidden neurons, is trained on a dataset of strong-motion records, such as SIMBAD v.6 (Smerzini *et al.*, 2014) or Next Generation Attenuation-West2 Project (Ancheta *et al.*, 2013), to predict short-period spectral ordinates ($T < T^*$) based on the long-period ones ($T \geq T^*$). Different ANNs are trained separately on the geometric mean of the horizontal components and on the vertical components for prediction of three-component ground motions.
2. For each simulated waveform, a target ANN2BB response spectrum is computed, the long-spectral ordinates of which, for $T \geq T^*$, coincide with the simulated ones, whereas they are obtained from the ANN for $T < T^*$ (separately for horizontal and vertical components). In our application, the corner period T^* is set depending on the frequency limitation of the numerical mesh. To preserve variability of the ANN results, the target at short periods is built on the median value calculated over 20 ANN realizations.
3. Once the ANN2BB target spectrum is defined for each waveform, the nonstationary stochastic approach by Sabetta and Pugliese (1996) is followed to generate the high-frequency portion of the signal. Updates of this approach (see e.g., Pousse *et al.*, 2006; Sabetta *et al.*, 2021) will be implemented in the next releases of the BB-SPEEDset. More specifically, 20

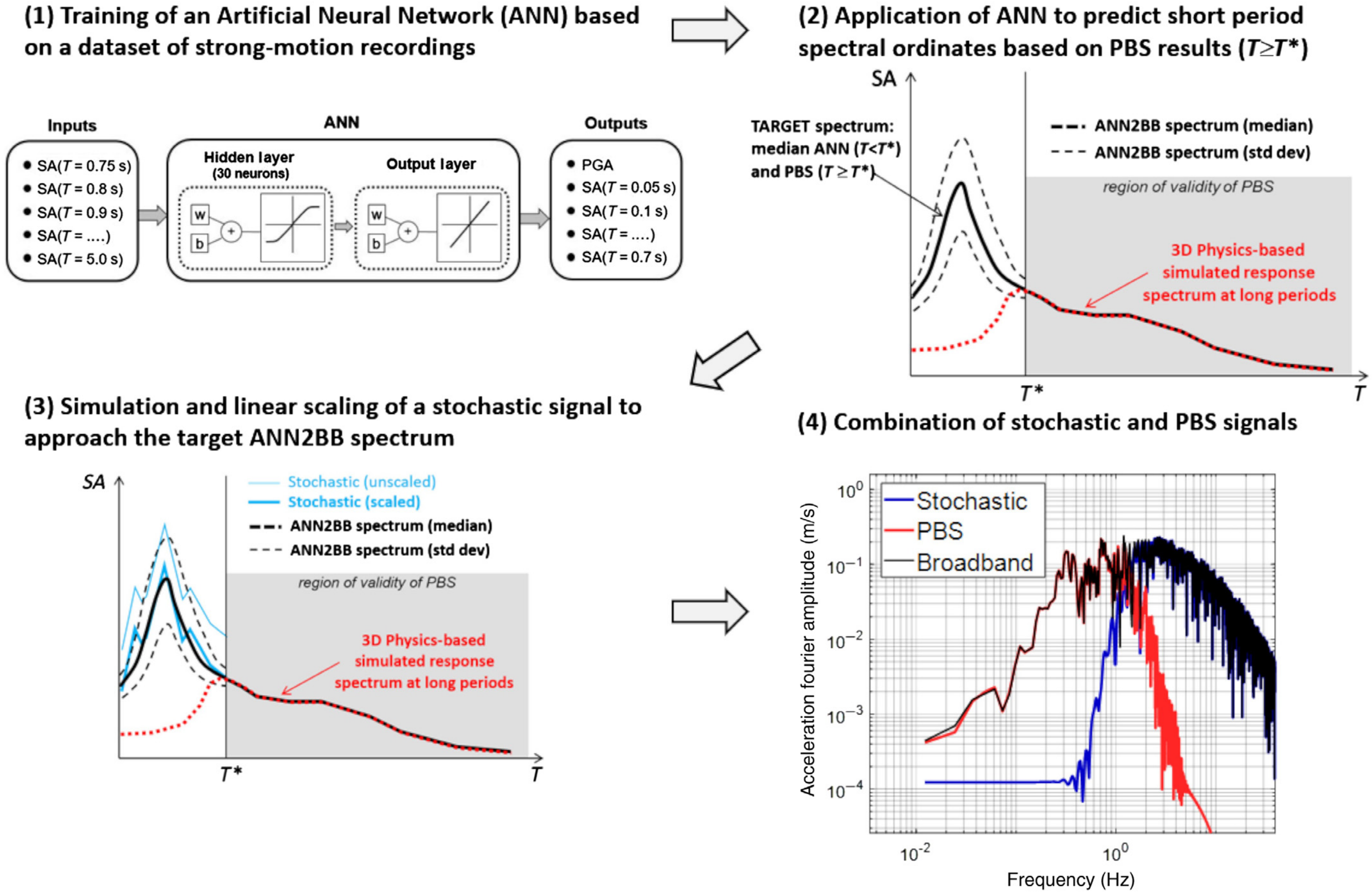

Figure 3. Flowchart of the ANN2BB approach revised after Paolucci *et al.* (2018) for the massive processing of physics-based numerical simulations (PBS) for broadband computation and compilation of BB-SPEEDset. The color version of this figure is available only in the electronic edition.

stochastic realizations are obtained, according to the simulated scenario (M_w) and receiver (distance, site conditions), and, out of these, a specific realization is selected based on the criteria illustrated in the sequel.

4. The selected stochastic signal (HF) and the PBS waveform (LF), previously filtered in the high- and low-frequency range, respectively, are combined in the time domain. Phase matching between HF and LF is achieved by alignment of the two time histories, according to the instant at 5% of normalized Arias intensity (I_A).

The scaling and selection of the stochastic signal of step (3) is based on a two-step procedure of minimization of the residuals with respect to the target ANN2BB spectrum. First, for each stochastic realization, a scaling factor *SF* that minimizes the residuals with respect to the target is calculated, and, subsequently, among the different scaled stochastic signal the one with the minimum misfit is selected. The optimum realization is obtained using the following minimization procedure:

$$\min_{j=1:n\mathrm{sim}} \left(\min_{SF} \sum_{i=1}^{N_{\mathrm{periods}}} w_i \left(\frac{\ln \mathrm{ANN}_{\mathrm{median},i} - \ln(SF \times \mathrm{STOCH}_i^j)}{\sigma_{\ln \mathrm{ANN},i}} \right)^2 \right), \quad (1)$$

in which *SF* is the scaling factor (typically in the range 0.5–2), N_{periods} are the vibration periods of the target ANN spectrum, w_i the weight for the i-th period, $n\mathrm{sim} = 20$ is the total number of stochastic signal realizations (20 realizations are found to guarantee a satisfying final spectrum). STOCH^j is the j-th stochastic realization. Both median ($\mathrm{ANN}_{\mathrm{median}}$) and standard deviation ($\sigma_{\ln \mathrm{ANN}}$) of the 20 ANNs are used to calculate the misfit. The weight vector w controls the fit to the target ANN spectrum. As the fit is actually performed only on the HF range, the weight vector takes the following values: $w = 0$ for $T > T^*$; $w = 1$ for $T < T^*$, and $w = 2$ for $T = T^*$. These values were selected after appropriate sensitivity analyses, to ensure that the final spectrum is "as close as possible" to the PBS one in the LF range, including the merging period, at the end of the procedure.

The main differences with respect to the procedure introduced by Paolucci *et al.* (2018) are the following:

- step 2: The target ANN2BB in the high-frequency range is computed as the median of 20 different ANN realizations,

TABLE 2
Structure of the BB-SPEEDset flat file

Source Metadata	Scenario ID	Hypocenter lat/lon/depth	Strike, dip, rake	Fault mechanism
	Event ID	M_w	References	Rupture top
	Scenario ID card	M_0	ANN_database	Fault vertices*
	Event_Time	Average slip	Transition period	Length*
	Event nation code	Number of segments	ANN2BB_procedure	Width*
Receiver Metadata	Receiver ID			
	Receiver east and north coordinates			
	Receiver elevation			
Site Response Proxies	V_{S30}	H_{bed} (depth of the alluvial-bedrock interface)	V_{Sbed} (time averaged V_S from the surface to H_{bed})	
	V_{Seq}	H_{800} (depth to $V_S \geq 800$ m/s)	V_{S800} (time averaged V_S from the surface to H_{800})	
Source-to-Site Distances†	Epicentral distance	R_line	Joyner and Boore distance, R_{JB}	
	Hypocentral distance	*Rx*	R_rup	
Intensity Measures‡	PGA	SA(*T*) for *T* from 0.01 to 10 s	Pulse-like flag	Housner intensity
	PGV	Permanent displacement	Pulse period	Arias intensity
	PGD	Mean period	Ds595, Ds575	Cumulative absolute velocity

PGA, peak ground acceleration; PGD, peak ground displacement; and PGV, peak ground velocity.
*Fault dimensions are given with respect to "numerical fault" and "effective fault."
†Distances from the fault are computed with respect to its "effective" dimensions.
‡Except pulse features, intensity measures are defined for the following directions: north–south, east–west, horizontal; up–down, vertical; HGM, horizontal geometrical mean; FN, fault normal; FP, fault parallel; D50, median value of the intensity measure (IM) distribution obtained from rotated waveforms; and D100, maximum value of the IM distribution obtained from rotated waveforms. (Rotation angles are given as well.)

rather than the output of a single ANN, to achieve a greater stability of results and minimize overfitting issues;

- step 3: The frequency scaling of the stochastic signal is replaced by a linear scaling in the time domain to approach the target ANN2BB spectrum at short periods. This improvement overcomes some issues related to the unrealistic frequency content that was sometimes introduced by the manipulation of Fourier spectra in the previous procedure. Furthermore, owing to its computational efficiency, it makes the broadband generation tool of SPEED suitable for massive computations over a very large number of receivers with no manual interventions, facilitating time-effective yet reliable outputs.

Finally, it is worth to remark two major advantages of the ANN2BB procedure with respect to other hybrid approaches to generate broadband signals based on PBS (see e.g., Mai and Beroza, 2003). First, since the resulting waveform is obtained based on the fit to a regular target response spectrum, it is possible to avoid the spurious discontinuities of the Fourier spectrum that are the typical result of the "glueing" of the physics-based (LF) signal with the stochastic one (HF), around a crossover frequency. Second, as thoroughly discussed by Paolucci *et al.* (2018), in the ANN2BB procedure the LF and HF portions are not independent, as for most hybrid approaches, but their correlation is enforced by the records-trained ANN. This allows the BB-SPEEDset results to be used to produce realistic earthquake ground-motion maps with the proper spatial correlation also at short periods, as it will be illustrated in the last section of this article for the case of the L'Aquila earthquake.

OVERVIEW OF THE BB-SPEEDSET: METADATA AND IMs

For each scenario and each selected receiver, a list of source metadata, postprocessing metadata, receiver metadata, site response proxies, source-to-site distances, and IMs are computed and stored in a flat file (see Table 2 for details). The fields of the flat file are consistent with the ones in the engineering strong motion (Lanzano *et al.*, 2018) and the NESS flat files (Sgobba *et al.*, 2021). However, when considering a database of PBS results, it is relevant to store information regarding the type of postprocessing accomplished, such as ANN training database, ANN transition period, broadband procedure, as done in BB-SPEEDset.

Because directional effects may be significant in the near-source region, each IM is defined on different horizontal directions, besides the vertical one, namely: the fault normal (FN) and fault parallel (FP) components, calculated rotating the horizontal waveforms orthogonal and parallel to the strike of the fault, respectively; the horizontal geometric mean (HGM), computed using the two horizontal east–west and north–south components; the maximum (RotD100) and the median (RotD50) values of IMs over all orientations (Boore, 2010), denoted in the following by D100 or D50, respectively. In addition to standard peak IMs, such as peak ground acceleration (PGA), peak ground velocity (PGV), peak ground

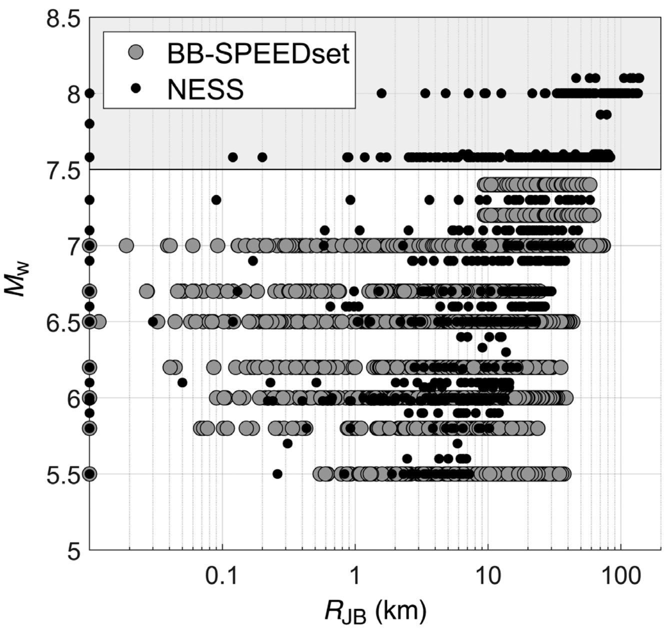

Figure 4. M_w and R_{JB} distribution of BB-SPEEDset (gray circles), in comparison with that from NEar-Source Strong-motion (NESS) dataset (black dots, after Sgobba *et al.*, 2021). The shaded region indicates the records excluded from the comparisons reported in this work.

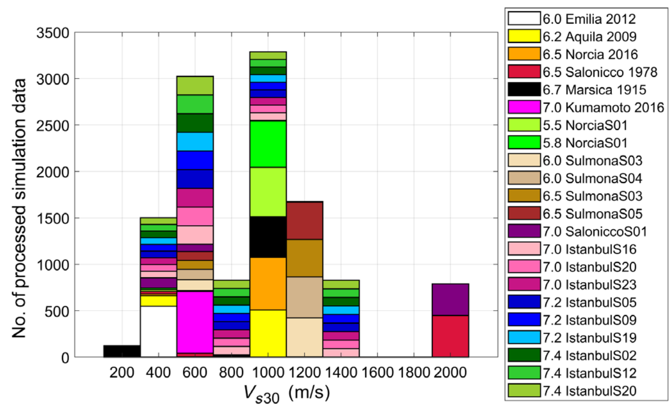

Figure 5. Distribution of BB-SPEEDset with respect to V_{S30}. The color version of this figure is available only in the electronic edition.

displacement (PGD), and response spectral accelerations (SA), a variety of integral- and frequency-related IMs is included, such as the Housner intensity (I_H), the cumulative absolute velocity (CAV), the Arias Intensity (I_A), the I_A -based durations (i.e., time interval between 5% and 95% of the total I_A, Ds595, and between 5% and 75% of the total I_A, Ds575; see Trifunac and Brady, 1975; Bommer and Martinez-Pereira, 1999) and the mean period (Rathje *et al.*, 1998). Furthermore, in the flat file compilation, special care was given to the characterization of pulse-like waveforms, which are of particular interest in earthquake engineering applications owing to their increased damage potential. Impulsive ground motions reflect two main physical effects. First, in forward-directivity conditions, the constructive superimposition of waves generated by a propagating rupture in front of a site may yield double-sided velocity pulses. Second, the contribution of waves generated by a finite dislocation on the fault plane can produce a permanent displacement (i.e., fling step), which results in a one-sided velocity pulse. As further discussed in the following, it is worth underlining that PBS can provide accurate predictions of displacement waveforms, including static offsets, which are hardly retrieved from recordings, because of the baseline drifts associated with errors in instrument response at low frequencies. The identification of pulse-like waveforms and of pulse period (T_p) has been done relying on the algorithm proposed by Shahi and Baker (2014). A thorough discussion on impulsive ground motions will be provided later in the article (see the Analysis of impulsive ground motions section).

The distribution of BB-SPEEDset data with respect to magnitude and distance is given in Figure 4. The dataset includes a total of 12,058 three-component waveforms from earthquake scenarios with M_w from 5.5 to 7.4 and Joyner–Boore distances (R_{JB}) up to 80 km. Strike-slip, normal, and thrust events are included in the dataset. Most records refer to normal (50%) and strike-slip (41%) focal mechanisms, whereas only 9% is from thrust earthquakes (i.e., only the 2012 Po Plain event; see Table 1). The dominance of normal and strike-slip faults is because, on one hand, normal events are typical of the seismicity in central Italy (mostly represented within the BB-SPEEDset), and, on the other hand, a significant set of strike-slip events from the North Anatolian fault (Istanbul case study, see Infantino *et al.*, 2021) and from the 2016 Kumamoto sequence (Sangaraju *et al.*, 2021) is also included.

In the same figure, the distribution of the NESS dataset is illustrated for comparison. Although the BB-SPEEDset does not cover yet earthquakes with $M_w \geq 7.5$ (and, for this reason, the comparisons shown hereafter will neglect this range), it can be seen that PBS allow to approach an ideally dense sampling at short distances that cannot be obtained by the NESS recording stations.

The distribution of BB-SPEEDset with respect to site conditions, parametrized in terms of the V_{S30}, is shown in Figure 5. About 40% of data correspond to soil conditions with $V_{S30} < 800$ m/s and about 60% to rock conditions, with dominance for hard-rock sites with V_{S30} larger than 1000 m/s. Within the soil classes, the majority of waveforms is on stiff soil with $V_{S30} > 400$ m/s, but an appreciable number of data are on very soft sites with V_{S30} as low as 150 m/s (Marsica case study). Figure 5 highlights another potential advantage of the simulated datasets: seismostratigraphic conditions are fully known in the PBS, so that each receiver may easily be associated to different proxies related to site response. Furthermore, site conditions that

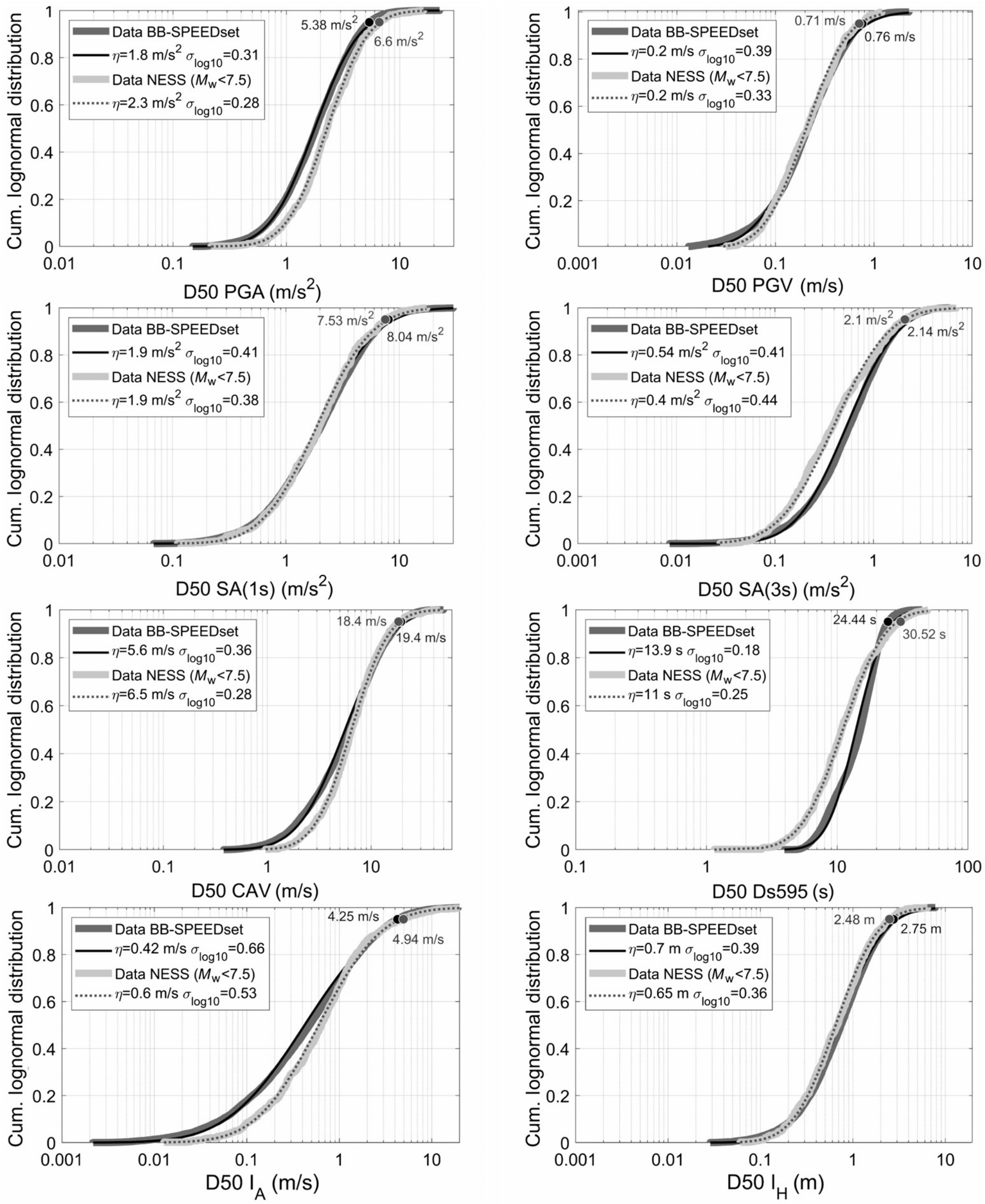

Figure 6. Cumulative distribution functions of peak ground acceleration (PGA), peak ground velocity (PGV), spectral acceleration (SA)(1.0 s), SA(3.0 s), cumulative absolute velocity (CAV), Ds595, Arias intensity (I_A), and Housner intensity (I_H), as obtained from BB-SPEEDset (dark gray: empirical; black: best-fitting lognormal distribution with corresponding statistical moments) and from NESS (light gray and dashed lines). The 95th percentiles of the statistical distributions are also superimposed on the graph. For all intensity measures (IMs), the D50 component is considered.

are typically poorly represented in the recorded datasets, such as rock and very soft sites, may be better sampled. This may provide further constraints, complementary to those from earthquake recordings, for the calibration of site amplification factors, especially in complex geological conditions.

As a final remark, BB-SPEEDset should be considered as a dynamically growing dataset, the scenarios of which may increase in a short time by extending to the case studies listed in Table 1 and not processed yet. Furthermore, new scenarios may specifically be developed to fill in the magnitude, distance, and site conditions gaps of the present version of BB-SPEEDset.

STATISTICAL DISTRIBUTIONS OF GROUND-MOTION IMs

As remarked in the Introduction, a crucial step for the potential use of the BB-SPEEDset flat file and signals for engineering applications is to compare the statistical distributions of different IMs, their attenuation with distance, the features of directional and impulsive near-source accelerograms, with those obtained from recorded ground motions, to verify the presence of potential biases and to identify their sources. For this purpose, because the SPEED results essentially refer to near-source conditions, we considered the NESS dataset introduced previously as a reference.

Figure 6 shows the cumulative distribution function of different IMs, namely, PGA, PGV, SA(1.0 s), SA(3.0 s), CAV, Ds595, I_A, and I_H, as computed from the entire BB-SPEEDset flat file. For all IMs, the D50 component is considered. To verify the consistency of our results against recordings, the statistical distributions derived from BB-SPEEDset are compared in Figure 6 with those obtained on the NESS dataset, within similar ranges of M_w and distances. As a matter of fact, for this comparison, only records with $M_w < 7.5$ are considered (corresponding to about 55% of NESS, see Fig. 4), consistently with BB-SPEEDset; note that, at low magnitude, larger distances are covered by BB-SPEEDset. To emphasize the comparison between the two independent sets of data, the lognormal distributions, fitting

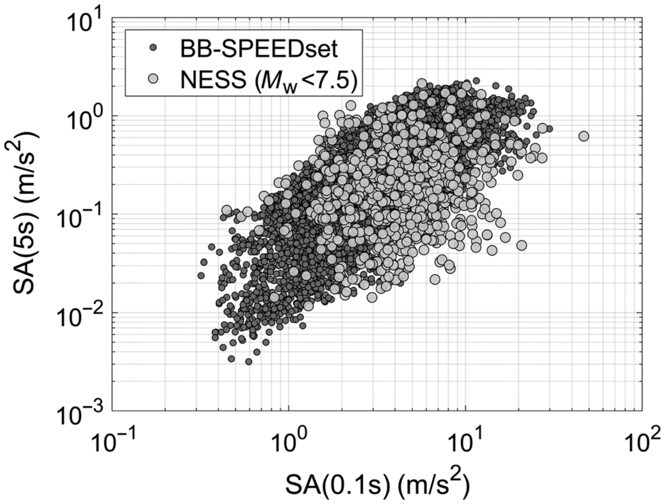

Figure 7. SA(0.1 s) and SA(5 s) distribution from BB-SPEEDset (dark gray) in comparison with that from NESS (light gray) in the same range of magnitude. The D50 component is considered for both spectral accelerations.

the empirical ones, are also superimposed, and the corresponding statistical moments are provided. Furthermore, for each IM distribution, the values of ground motion with a probability of exceedance less than 5% (i.e., 95th percentile of the related distributions) are highlighted on the graph. Overall, it is remarkable that a full consistency is found between BB-SPEEDset and NESS, as it should be, as the distribution of M_w and R_{JB} of the two datasets are also consistent (apart from slight differences, as commented earlier). Although the BB-SPEEDset tends to underestimate the recorded values of PGA by a factor of about 20%, probably owing to the difficulty of the ANN2BB approach to describe the short periods as accurately as the long periods, the statistical distributions of several IMs, from peak measures to integral ones, are noticeably similar both in terms of median and standard deviation ($\sigma_{\log 10}$). The agreement of PGV, SA (1.0 s), CAV, and I_H is excellent. For SA(3.0 s), BB-SPEEDset tends to provide more severe ground motions, most likely because of the intrinsic higher coherency of waveforms simulated by means of numerical models that inevitably cannot account for the actual small-scale heterogeneities and complexities in the source, path, and site. Referring to I_A, some discrepancies are found especially at intensity values lower than the median values (median from BB-SPEEDset is lower than NESS of a factor of about 25%), but the agreement improves significantly above the median. As a matter of fact, the 95th percentiles from BB-SPEEDset and NESS differ of less than 10%. Although the standard deviations from BB-SPEEDset and NESS are comparable in most cases, differences are found for the duration Ds595, being $\sigma_{\log 10}$ from BB-SPEEDset lower (0.18) with respect to the one from NESS (0.25), suggesting that the level of waveform complexity achieved through SPEED simulations is still lower than reality.

As a further consistency check, the distribution of SA(0.1 s) and SA(5.0 s) obtained from BB-SPEEDset is compared with that from NESS (M_w < 7.5) in Figure 7. It turns out that the correlation between long and short periods of BB-SPEEDset (the latter ones being a direct output of the ANN2BB procedure described previously) is consistent with the one from NESS, with few exceptions of NESS values having a combination of high short-period and low long-period spectral ordinates, not present in the simulated waveforms.

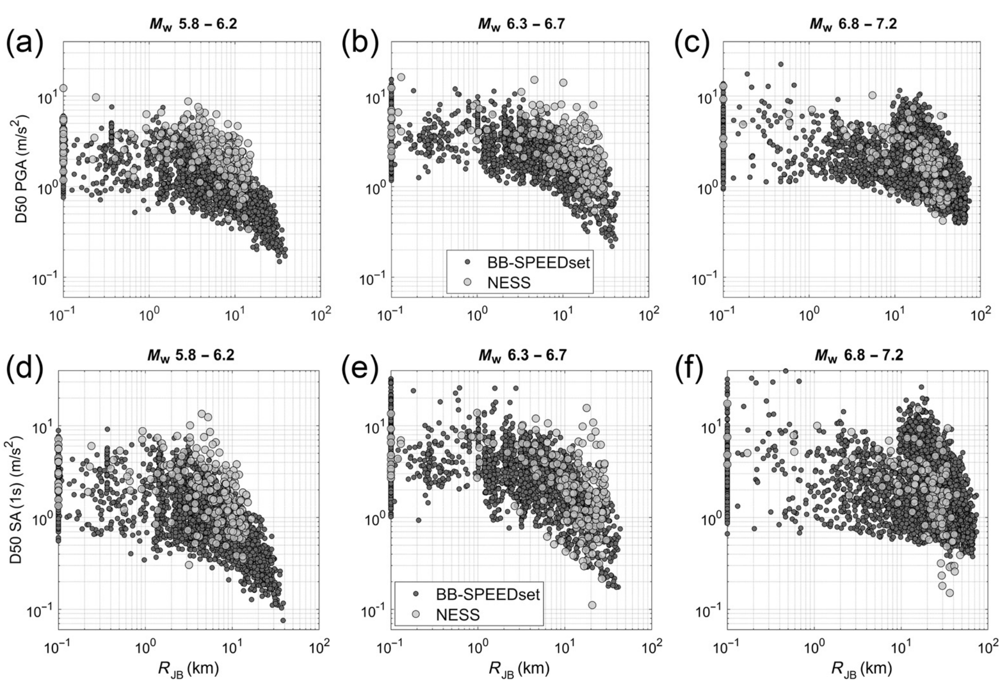

Figure 8. D50 components of (a–c) PGA and (d–f) SA (1 s) (bottom) as a function of R_{JB} distance, for BB-SPEEDset (dark gray) and NESS (light gray), considering different M_w ranges (centered around 6.0, 6.5, and 7.0).

GROUND-MOTION ATTENUATION WITH DISTANCE

Attenuation of ground-motion IMs with distance for the BB-SPEEDset and NESS are compared in this section. Figure 8 shows PGA and SA(1 s) as a function of R_{JB}, using D50 component, for different M_w ranges. No discrimination of soil conditions has been made. The agreement is reasonably good, with a similar trend of IMs with distance. As already mentioned, there is a tendency of PGAs of the BB-SPEEDset to lie on

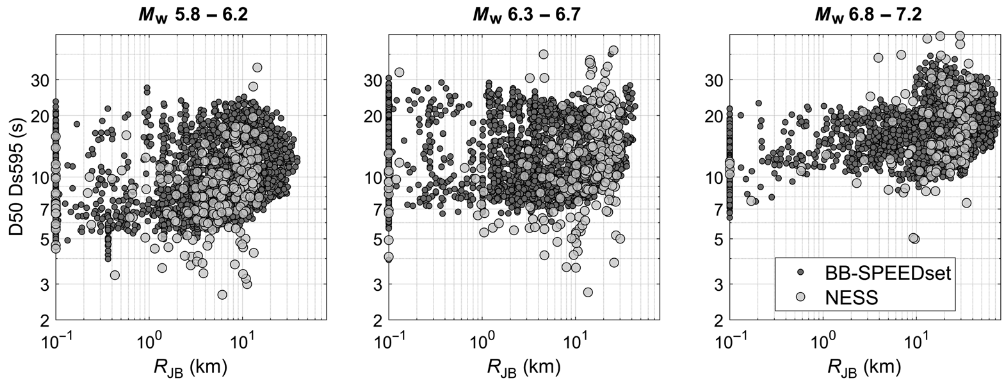

Figure 9. Duration Ds595 (for D50 component) versus R_{JB} distance, for both BB-SPEEDset (dark gray) and NESS (light gray), for different M_w ranges (centered around 6.0, 6.5, and 7.0).

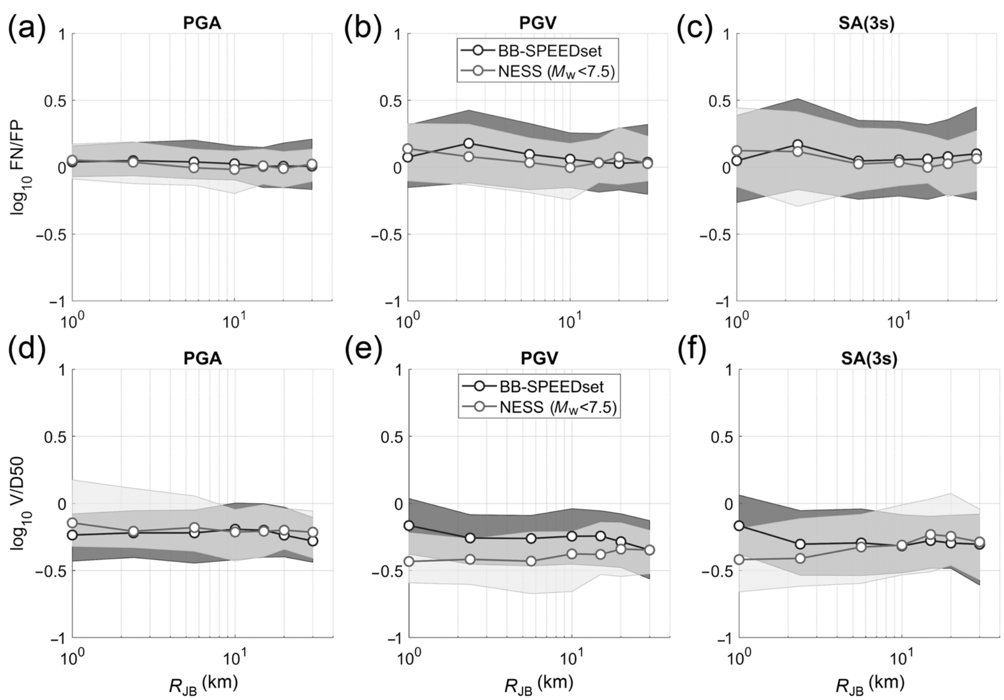

Figure 10. Ratios of (a–c) fault normal and fault parallel (FN/FP) and of (d–f) V/D50 for PGA (left), PGV (center), and SA (3 s) (right), as a function of R_{JB}. The median $\pm\sigma$ ratios from BB-SPEEDset (dark gray) and NESS (light gray) are compared.

the lower side of recorded values, especially in the lower M_w range. Spectral ordinates at intermediate periods, SA(1 s), show a better agreement with NESS, at any distance. A large but comparable scatter can be observed for the two datasets, slightly larger for SA(1 s). The larger scatter for M_w around 7.0 and $R_{JB} > 10$ km is related to the Istanbul simulations that do not have receivers at shorter distances from the source. The high spectral accelerations from NESS at 1 s for M_w in the 6.3–6.7 range and $R_{JB} > 10$ km are mostly related to the 1994 Northridge earthquake, whereas the lowest values (in the same M_w and R_{JB} ranges) are for the 2014 Aegean Sea earthquake of M_w 6.4. The very low SA(1 s) values for M_w in the 6.8–7.2 range and $R_{JB} > 20$ km are related to the Japanese earthquake of 2008.

Figure 9 shows attenuation with R_{JB} for the Ds595 duration of ground motion. Again, an overall good agreement among the two datasets is noticeable, with NESS records showing a greater scatter probably because of their higher complexity than simulated waveforms, as previously noted. Except for this remark, simulated durations provide a consistent trend with magnitude and distance.

DIRECTIONALITY AND VERTICAL-TO-HORIZONTAL MOTIONS

It is widely recognized that earthquake ground motion may exhibit specific features in proximity of the source (e.g., Stewart *et al.*, 2001), including polarization related to the fault mechanism and large, short-period, vertical components exceeding, even significantly, the corresponding horizontal ones (Bommer *et al.*, 2011; Gülerce and Abrahamson, 2011). These aspects will be addressed in this section, with special care again to the comparison with recordings.

igure 10 shows the median ($\pm\sigma$, shaded regions) FN/FP (Fig. 10a–c) and V/D50 (Fig. 10d–f) for PGA, PGV, and SA(3 s), as a function of R_{JB}, as obtained from BB-SPEEDset and NESS ($M_w < 7.5$). Although long-period components of ground motion are directly related to the PBS results, short-period components, such as PGA, reflect the output of the ANN2BB procedure. Referring to the FN/FP distribution, an excellent agreement is found both in terms of median value and variability at different distances from the source. As expected, both datasets show

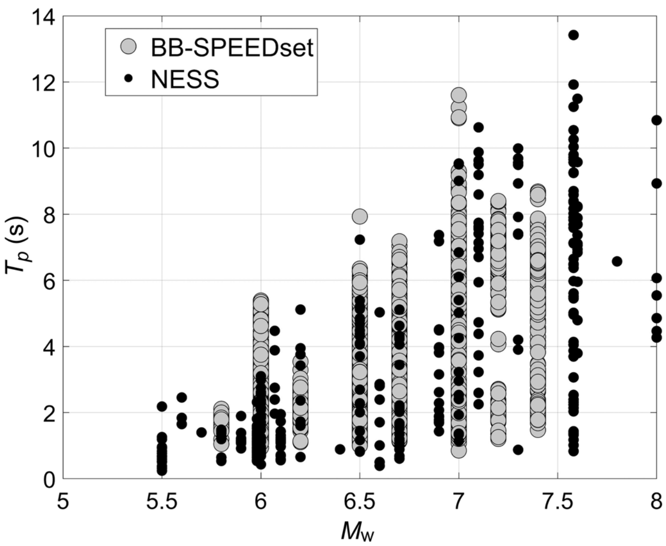

Figure 11. Pulse period T_p versus earthquake magnitude for observed pulse-like ground motions of BB-SPEEDset (20% of set data, in light gray) and NESS dataset (almost 30% of whole set data, in black).

that in near-source conditions the FN motion is stronger than the FP at intermediate and long periods and at very short distance, $R_{JB} < 5$ km. At increasing distances, the FN polarization tends to vanish, in agreement with previous studies (Somerville *et al.*, 1997; Pacor *et al.*, 2018). On the other hand, at short periods, no polarization effects are found, with median FN/FP ratios equal to approximately one at all distances, both in BB-SPEEDset and in NESS. Especially at long periods, the variability across periods is rather large, meaning that directionality features are region- and scenario-specific. Here, the variability of simulated waveforms tends to be slightly larger, but differences remain limited. Further insights on the physical reasons of such variability could be obtained by analyzing the dependence on the focal mechanism and the spatial distribution of such ratios for specific rupture scenarios.

As regards to the V/D50 ratios, there is a good agreement in terms of PGA (median V/D50 ~ 0.6 for both datasets, but with larger variability for NESS), whereas for PGV and SA(3 s) the BB-SPEEDset values at very short distance (median V/D50 ~ 0.6) are higher than NESS (median V/D50 ~ 0.4). More detailed studies are planned to investigate the dependence of such different ratios on the focal mechanism and site conditions.

ANALYSIS OF IMPULSIVE GROUND MOTIONS

This section focuses on the identification and comparison of pulse signals, together with the corresponding period T_p, tagged and stored in both BB-SPEEDset and NESS flat files.

Figure 11 shows T_p values calculated following the algorithm proposed by Shahi and Baker (2014) as a function of magnitude, for both BB-SPEEDset and NESS. T_p ranges from 1 to 12 s, with amplitudes tending to increase with magnitude (Mavroeidis and Papageorgiou, 2003; Somerville, 2003), but with the largest values probably related to coupling with deep basin conditions, such as for the earthquakes of M_w 6.0 Po Plain, and M_w 6.7 Marsica, that are poorly represented by the NESS dataset. With these limitations in mind in terms of comparison of datasets, the agreement of the T_p trends from the two datasets is remarkable.

Figure 12 shows the trend of T_p as a function of the ratio between PGD and PGV (*PGD/PGV*), for NESS (Fig. 12a) and BB-SPEEDset (Fig. 12b). A reasonably good agreement between the two sets is found within comparable magnitude ranges (i.e., M_w from 6.0 to 7.4). To improve the accuracy of the PGD estimations from the NESS dataset, T_p and peak values from the e-BASCO baseline corrected waveforms have been considered (see Sgobba *et al.*, 2021 for details).

Closed-form analytical relationships between T_p and *PGD/PGV* are also shown in Figure 12, with thick black and gray lines, calculated based on simple functions that may approximate impulsive ground motion. These relationships are based on the analytical expressions of the Fourier spectra of the "Ricker wavelet" and of the "double-impulse" functional forms, given by (for unit peak amplitude):

$$\text{Ricker wavelet}: v(t) = (1 - 2\alpha^2 t^2)e^{-\alpha^2 t^2} \quad \text{with} \quad \alpha = \pi f_p, \tag{2a}$$

$$\text{Double-impulse}: v(t) = 2\pi f_p \sqrt{e} t e^{-\alpha^2 t^2} \quad \text{with} \quad \alpha = \sqrt{2}\pi f_p, \tag{2b}$$

for which the peak of the Fourier spectrum corresponding to the frequency $f_p = 1/T_p$ can be identified and related to PGV and PGD, as shown in the top right of Figure 12. It is interesting that most data from both sets fall between the two analytical relationships, suggesting that the variability of impulsive ground motions may roughly be represented by these two functional families.

QUERY BY EARTHQUAKE OF THE BB-SPEEDset: THE L'AQUILA EXAMPLE

In this section, we highlight the information that can be obtained from BB-SPEEDset by selecting a specific earthquake (query by earthquake) and extracting the corresponding waveforms and IMs. As an explanatory case study, the 6 April 2009 M_w 6.2 L'Aquila earthquake is considered.

First, as a set of illustrative results of the ANN2BB procedure, Figure 13 shows the broadband three-component (east–west, north–south, and up–down) acceleration, velocity, and displacement time histories at selected receivers, superimposed on the corresponding PGA, PGV, and PGD maps. Referring to

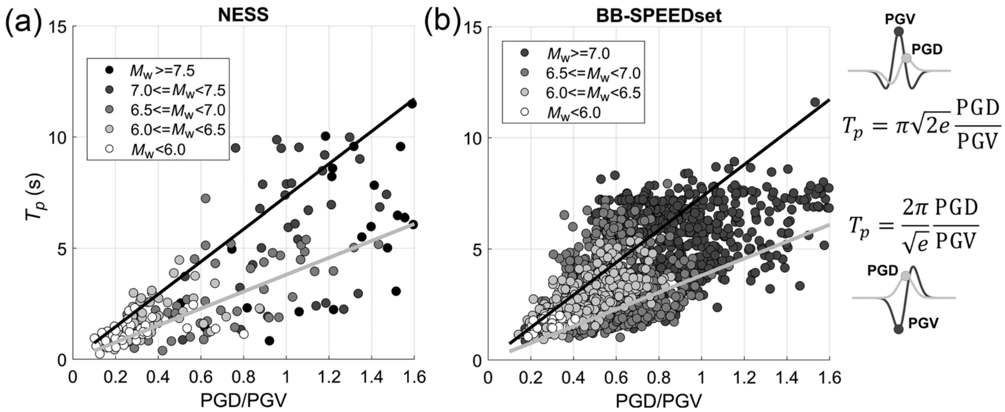

Figure 12. Pulse period T_p as a function of *PGD/PGV* for (a) NESS and for (b) BB-SPEEDset, for different magnitude ranges, together with analytical relationships for Ricker wavelet and double-impulse functions.

Smerzini and Villani (2012) and Evangelista *et al.* (2017) for a thorough comparison of recorded and simulated waveforms, it is noted herein that simulated time histories have realistic features in terms of duration, amplitudes, and frequency content, with displacement waveforms showing permanent displacements related to the coseismic slip on the fault. Furthermore, the spatial distribution of peak ground motion values at high frequency (PGA) turns out to be well correlated with the geological features of the basin (see areas of maximum amplitudes within the basin), supporting the effectiveness of the ANN2BB approach in establishing a correlation between long- and short-period ordinates, and, thus, reproducing at short periods physics-based features that are simulated only at long periods. It is also interesting to note that, moving from maps related to short periods (PGA) to those related to long periods (PGD), the spatial correlation of ground motion appears to be characterized by increasing correlation length, as expected, at least from a qualitative point of view. Quantitative evaluations of spatial correlation of spectral accelerations from broadband numerical simulations can be found in Infantino, Smerzini, and Lin (2021) and in Schiappapietra and Smerzini (2021).

To appreciate the richness of information included in BB-SPEEDset flat file, Figure 14 shows, for the same case study of L'Aquila, the maps of different IMs, namely, PGV, CAV, I_A, T_p, I_H, and Ds595. The FN component is shown for all IMs, except for T_p, which is computed for the orientation in which the pulse is the strongest according to the algorithm by Shahi and Baker (2014).

One of the main outcomes of BB-SPEEDset is related to the possibility of drawing maps and making quantitative evaluations of spatial correlation of a broad spectrum of IMs, for any orientation of ground motion, with a level of detail that could not be possible using recordings owing to their limited number. From the maps of Figure 14, the following comments can be made:

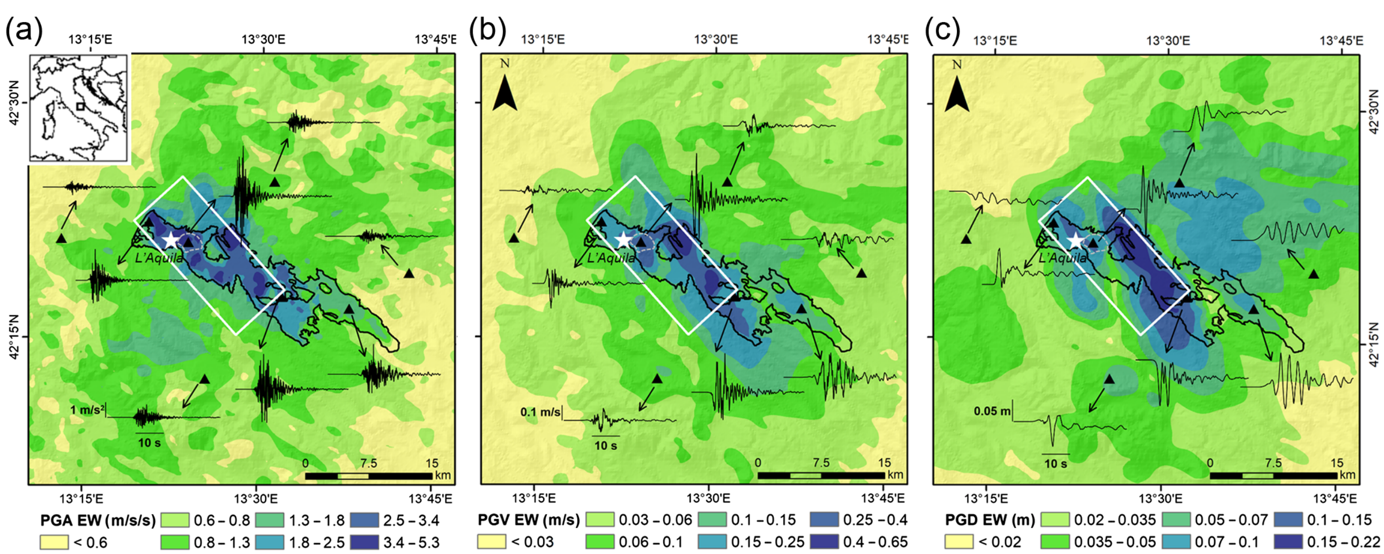

Figure 13. 2009 M_w 6.2 L'Aquila: peak ground motion maps (a) PGA, (b) PGV, and (c) PGD and selected broadband waveforms (left: acceleration; center: velocity; right: displacement), east–west component, from BB-SPEEDset. The thick contour represents the shape of the Aterno River basin, whereas the dashed contour denotes the location of the L'Aquila historical center. The inset in (a) shows the location of the map within Italy. The color version of this figure is available only in the electronic edition.

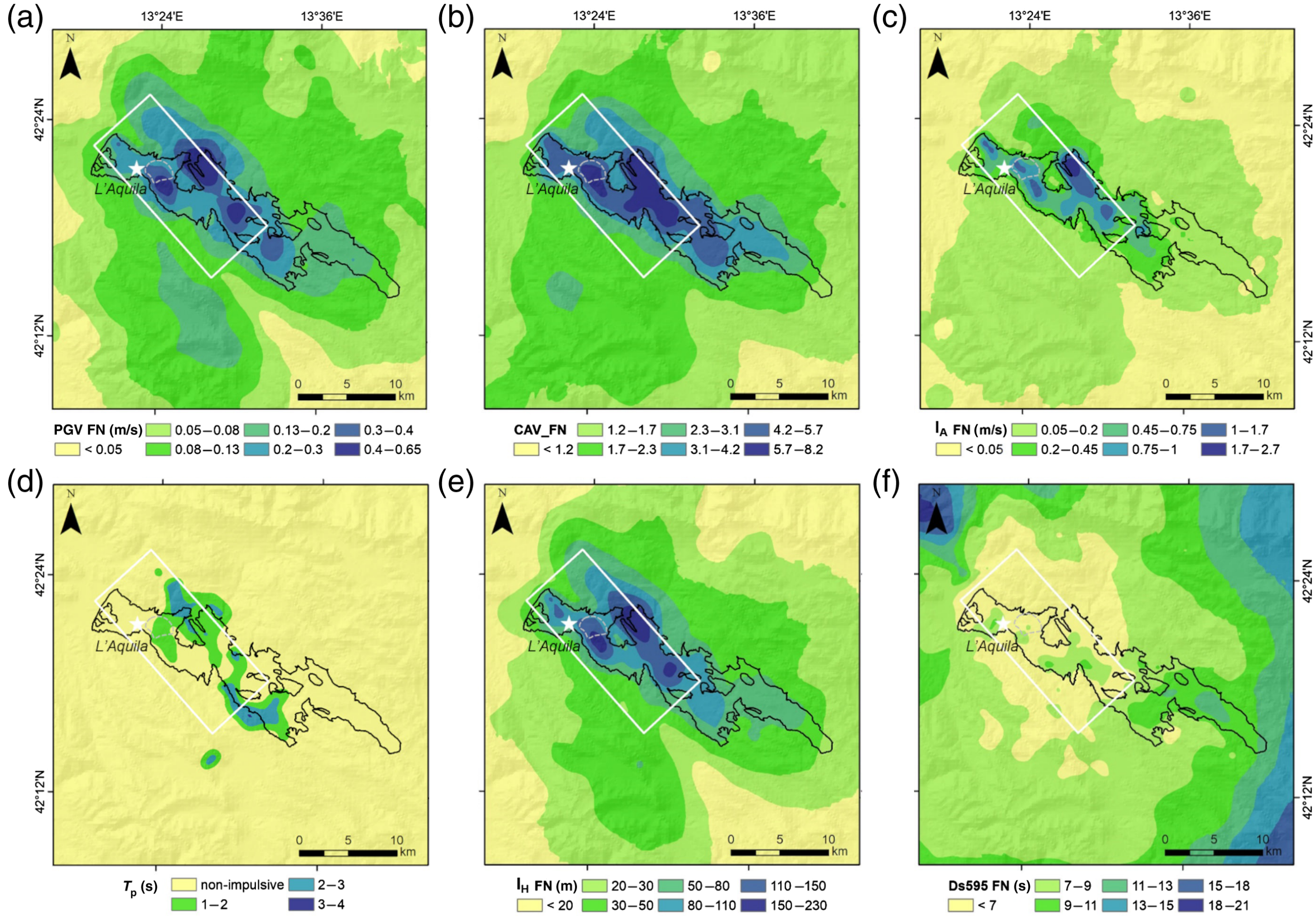

Figure 14. 2009 M_w 6.2 L'Aquila: maps of different ground motion IMs stored in BB-SPEEDset, (a) PGV, (b) CAV, (c) I_A, (d) pulse period T_p, (e) I_H, and (f) Ds595. For all IMs, except T_p, the FN component is shown. The color version of this figure is available only in the electronic edition.

- areas of maximum intensity of PGV, CAV, I_H, and I_A are concentrated on the surface projection of the fault and inside the alluvial basin, because of the coupling of site response with rupture propagation effects;
- lobes of maximum CAV correlate well with the shape of the basin, also at its southeastern edge;
- there is an overall similarity between the spatial patterns of PGV and I_H, which is not obvious from their definitions: the former is an instantaneous measure of ground shaking, whereas the latter, defined as the area of the pseudovelocity spectrum (5% damping in this case) between 0.1 and 2.5 s, is proportional to the maximum kinetic energy stored in an elastic structure;
- the areas of pulse-like ground-motion occurrence are found typically close the top edge of the fault, mostly related to up-dip directivity effects, highlighting an interesting correlation between strong pulse-like motions with the areas of peak values for the FN component (see left panels of Fig. 14.);
- correspondingly to areas with impulsive motions, the lowest values of ground-motion duration are found.

Although these comments may be considered to be specific for the L'Aquila earthquake case study, they convey the idea of the comprehensive picture of earthquake ground motion that can be obtained from PBS and of the potential outcomes that the analysis of the simulated waveforms may provide in terms of an improved characterization of near-source ground shaking. As a further example, Figure 15 shows the maps of permanent displacement D_{perm} computed from BB-SPEEDset for the L'Aquila case study, along the FP, FN, and UD components. Although the fling step is naturally reproduced by physics-based simulation of seismic-wave propagation, the estimation of permanent displacement from earthquake recordings requires complex signal processing procedures (D'Amico *et al.*, 2019), which are typically subject to high uncertainties. This points out one of the main advantages of numerical simulations, that is, to provide an accurate and detailed picture of the long-period components of earthquake ground motion, with relevant implications for the calibration

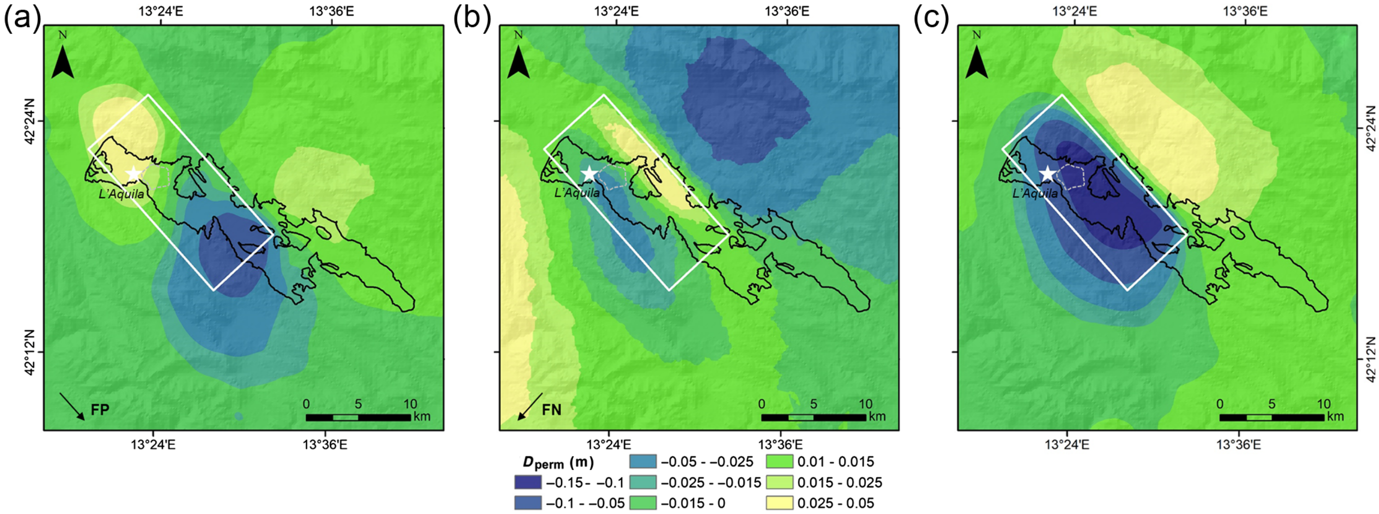

Figure 15. 2009 M_w 6.2 L'Aquila: maps of permanent displacement (D_{perm}) on the three components of motion, (a) FP, (b) FN, and (c) up–down (UD). The color version of this figure is available only in the electronic edition.

of GMMs for PGD and displacement spectral ordinates (Cauzzi *et al.*, 2015).

Coherently with the normal focal mechanism of the Paganica fault, responsible of the L'Aquila earthquake, the ground underwent a static maximum horizontal offset of around 10 cm (both on the footwall and hanging wall along the FN and FP directions, respectively) and a maximum subsidence of about 15 cm on the hanging wall. The latter is consistent with the maximum coseismic vertical displacement obtained from both Differential Interferometric Synthetic Aperture Radar and Global Positioning System observations (D'Agostino *et al.*, 2012).

CONCLUSIONS

In this article, we have presented the BB-SPEEDset—a new dataset of near-source broadband earthquake ground motions from 3D PBS obtained by the spectral element computer code SPEED. This is expected to support research on the characterization of earthquake ground motions in the proximity of the seismic source and in complex geological conditions that cannot be extensively documented based on available records.

To produce the dataset, an effective workflow has been devised to postprocess raw PBS results in a homogeneous and repeatable format. The core of the workflow is the generation of broadband ground motions starting from PBS results, reliable only in the low-frequency range, according to the ANN2BB procedure first proposed in Paolucci *et al.* (2018) and further improved in this work to make it suitable for massive processing of simulated waveforms.

At the present stage, BB-SPEEDset consists of a total number of 12,058 three-component waveforms from worldwide earthquake scenarios, mostly validated against records, with M_w from 5.5 to 7.4 and R_{JB} up to 80 km. Besides source, receiver, and postprocessing metadata, the BB-SPEEDset flat file can provide a large portfolio of ground-motion IMs, from the standard peak and spectral measures to integral ones (e.g., I_H, CAV, duration, I_A), up to parameters related to impulsive ground motions (e.g., pulse period T_p) and long-period components of ground motions such as D_{perm}.

An extensive set of checks has been performed and documented in this article to verify that the BB-SPEEDset provides peak values, integral IMs, ratios of long-to-short period spectral ordinates, features of impulsive ground motions and directionality effects, consistent on a statistical basis with NESS—a dataset of worldwide near-source records (Sgobba *et al.*, 2021). The positive outcome of such consistency check was not obvious, because the BB-SPEEDset is the last step of a series of complex studies, starting from the construction of large-scale 3D numerical models, the simulation of realistic fault-rupture scenarios, the source-to-site propagation of seismic waves in complex geological media, and, finally, a smart postprocessing of low-frequency signals to get broadband waveforms using ANN. Although reproducing exactly the recorded ground motions by PBS is not an achievable objective, this article shows that it is possible to construct realistic earthquake ground-motion scenarios, and that the resulting waveforms are consistent in terms of peak values, duration and frequency content, with records obtained in near-source conditions.

Given this major outcome, we envisage that the BB-SPEEDset, either in the present version or in the following ones enriched by further simulated scenarios, will serve as the basis for several new achievements for an improved characterization and engineering usage of near-source earthquake ground motions, such as:

- to fill in the gaps, in terms of source-to-site conditions, focal mechanisms, variability of fault-slip distributions and directivity effects, complex geological conditions that are present in the worldwide near-source records datasets and that are not expected to be easily covered in short time by additional records;

- in the conditions above, provide region- and site-specific input motions for nonlinear structural analyses of engineered structures that are presently often carried out using unrealistic scaling factors on recorded ground motions;
- to provide accurate predictions of long-period components of ground motions, including PGDs and static offsets, that are hardly retrieved from records because of the uncertainties associated with the postprocessing procedures;
- to construct region-specific scenarios of earthquake ground shaking, suitable to improve empirical models of spatial correlation (Infantino, Smerzini, and Lin, 2021) and spatial coherency of ground motion (Smerzini, 2018), taking advantage of the dense spacing of receivers that can be achieved in the numerical modeling;
- to support the development of nonergodic models for ground-shaking scenarios as a key tool for enhanced seismic hazard and seismic risk evaluations in large urban areas (Stupazzini *et al.*, 2021).

DATA AND RESOURCES

The NEar-Source Strong-motion version 2.0 (NESS2.0) dataset has been downloaded at http://ness.mi.ingv.it/ (last accessed March 2021). The BB-SPEEDset (v.1.0) is available at http://speed.mox.polimi.it/BB-SPEEDset (last accessed May 2021), in which both the flat file and corresponding broadband waveforms can be downloaded. The open-source Spectral Element code SPEED is available at http://speed.mox.polimi.it (last accessed July 2021).

DECLARATION OF COMPETING INTERESTS

The authors acknowledge that there are no conflicts of interest recorded.

ACKNOWLEDGMENTS

This work has been partially supported by swissnuclear within the research activity “Development of advanced numerical approaches for earthquake ground motion prediction,” in the framework of the SIGMA2 project, and by the Department of Civil Protection within the ReLUIS project WP18 “Normative contributions related to seismic action.” The authors wish to thank in particular, Marco Stupazzini, Ilario Mazzieri, Maria Infantino, and Karim Tarbali, together with the entire SPEED team, for their support in the development of SPEED kernel, of the related pre- and postprocessing tools and for their contributions to the simulation of some of the earthquake scenarios that this work has been based on. The fruitful discussions with Philippe Renault in the framework of the swissnuclear-SIGMA2 project are also gratefully acknowledged. Constructive comments by Thomas Pratt, Francesca Pacor, and by another anonymous reviewer helped improving the article and are gratefully acknowledged.

REFERENCES

Ancheta, T. D., R. B. Darragh, J. P. Stewart, E. Seyhan, W. J. Silva, B. S. J. Chiou, K. E. Wooddell, R. W. Graves, A. R. Kottke, D. M. Boore, *et al.* (2013). *PEER NGA-West2 Database*, PEER Report No. 2013/03, Pacific Earthquake Engineering Research Center, University of California, Berkeley, California, 134 pp.

Antonietti, P. F., I. Mazzieri, L. Melas, R. Paolucci, A. Quarteroni, C. Smerzini, and M. Stupazzini (2020). Three-dimensional physics-based earthquake ground motion simulations for seismic risk assessment in densely populated urban areas, *Math. Eng.* **3,** no. 2, 1–31, doi: 10.3934/mine.2021012.

Baker, J. W., S. Rezaeian, C. A. Goulet, N. Luco, and G. Teng (2021). A subset of CyberShake ground-motion time series for response-history analysis, *Earthq. Spectra* doi: 10.1177/8755293020981970.

Bielak, J., R. W. Graves, K. B. Olsen, R. Taborda, L. Ramirez-Guzman, S. M. Day, G. P. Ely, D. Roten, T. H. Jordan, P. J. Maechling, *et al.* (2010). The ShakeOut earthquake scenario: Verification of three simulation sets, *Geophys. J. Int.* **180,** no. 1, 375–404.

Bommer, J. J., and A. Martinez-Pereira (1999). The effective duration of earthquake strong motion, *J. Earthq. Eng.* **3,** 127–172.

Bommer, J. J., S. Akkar, and Ö. Kale (2011). A model for vertical-to-horizontal response spectral ratios for Europe and the Middle East, *Bull. Seismol. Soc. Am.* **101,** no. 4, 1783–1806.

Boore, D. M. (2010). Orientation-independent, nongeometric-mean measures of seismic intensity from two horizontal components of motion, *Bull. Seismol. Soc. Am.* **100,** 1830–1835.

Bracewell, R. N. (1986). *The Fourier Transform and Its Applications*, Second Ed., McGraw-Hill, New York, New York.

Bradley, B. A., D. Pettinga, J. W. Baker, and J. Fraser (2017). Guidance on the utilization of earthquake-induced ground motion simulations in engineering practice, *Earthq. Spectra* **33,** no. 3, 809–835.

Bradley, B. A., K. Tarbali, R. L. Lee, J. Huang, J. Motha, S. E. Bae, V. Polak, M. Zhu, C. Schill, J. Patterson, and D. Lagrava (2020). Cybershake NZ v19.5: New Zealand simulation-based probabilistic seismic hazard analysis, *Proc. of the 2020 New Zealand Society for Earthquake Engineering Annual Technical Conference*, Wellington, New Zealand, 22–24 April.

Cauzzi, C., E. Faccioli, M. Vanini, and A. Bianchini (2015). Updated predictive equations for broadband (0.01–10 s) horizontal response spectra and peak ground motions, based on a global dataset of digital acceleration records, *Bull. Earthq. Eng.* **13,** 1587–1612, doi: 10.1007/s10518-014-9685-y.

Chaljub, E., P. Moczo, S. Tsuno, P. Y. Bard, J. Kristek, M. Kaser, M. Stupazzini, and M. Kristekova (2010). Quantitative comparison of four numerical predictions of 3D ground motion in the Grenoble valley, France, *Bull. Seismol. Soc. Am.* **100,** no. 4, 1427–1455.

D’Agostino, N., D. Cheloni, G. Fornaro, R. Giuliani, and D. Reale (2012). Space–time distribution of afterslip following the 2009 L’Aquila earthquake, *J. Geophys. Res.* **117,** no. B2, doi: 10.1029/2011JB008523.

D’Amico, M., C. Felicetta, E. Schiappapietra, F. Pacor, F. Gallovič, R. Paolucci, R. Puglia, G. Lanzano, S. Sgobba, and L. Luzi (2019). Fling effects from near-source strong-motion records: Insights from the 2016 Mw 6.5 Norcia, Central Italy, earthquake, *Seismol. Res. Lett.* **90,** no. 2A, 659–671.

D’Amico, M., R. Puglia, E. Russo, C. Maini, F. Pacor, and L. Luzi (2017). SYNTHESIS: A web repository of synthetic waveforms, *Bull. Earthq. Eng.* **15,** 2483–2496.

Evangelista, L., S. Del Gaudio, C. Smerzini, A. D’Onofrio, G. Festa, I. Iervolino, L. Landolfi, R. Paolucci, A. Santo, and F. Silvestri (2017).

Physics-based seismic input for engineering applications: A case study in the Aterno River valley, Central Italy, *Bull. Earthq. Eng.* **15,** no. 7, 2645–2671.

Fayaz, J., S. Rezaeian, and F. Zareian (2021). Evaluation of simulated ground motions using probabilistic seismic demand analysis: CyberShake (ver. 15.12) simulations for Ordinary Standard Bridges, *Soil Dynam. Earthq. Eng.* **141,** no. 106533, 1–12.

Galasso, C., P. Zhong, F. Zareian, I. Iervolino, and R. W. Graves (2013). Validation of ground-motion simulations for historical events using MDoF systems, *Earthq. Eng. Struct. Dynam.* **42,** no. 9, 1395–1412.

Gatti, F., S. Touhami, F. Lopez-Caballero, R. Paolucci, D. Clouteau, V. A. Fenrnandes, M. Kham, and F. Voldoire (2018). Broad-band 3-D earthquake simulation at nuclear site by an all-embracing source-to-structure approach, *Soil Dynam. Earthq. Eng.* **115,** 263–280.

Graves, R. W., and A. Pitarka (2010). Broadband ground-motion simulation using a hybrid approach, *Bull. Seismol. Soc. Am.* **100,** 2095–2123.

Graves, R. W., and A. Pitarka (2015). Refinements to the Graves and Pitarka (2010) broadband ground-motion simulation method, *Seismol. Res. Lett.* **86,** 75–80.

Graves, R. W., T. H. Jordan, S. Callaghan, E. Deelman, E. H. Field, G. Juve, C. Kesselman, P. Maechling, G. Mehta, K. Milner, *et al.* (2011). CyberShake: A physics-based seismic hazard model for Southern California, *Pure Appl. Geophys.* **168,** 367–381, doi: 10.1007/s00024-010-0161-6.

Guidotti, R., M. Stupazzini, C. Smerzini, R. Paolucci, and P. Ramieri (2011). Numerical study on the role of basin geometry and kinematic seismic source in 3D ground motion simulation of the 22 February 2011 M_w6.2 Christchurch earthquake, *Seismol. Res. Lett.* **82,** no. 6, 767–782.

Gülerce, Z., and N. A. Abrahamson (2011). Site-specific design spectra for vertical ground motion, *Earthq. Spectra* **27,** no. 4, 1023–1047.

Herrero, A., and P. Bernard (1994). A kinematic self-similar rupture process for earthquakes, *Bull. Seismol. Soc. Am.* **84,** 1216–1229.

Imperatori, W., and F. Gallovič (2017). Validation of 3D velocity models using earthquakes with shallow slip: Case study of the M_w6.0 2014 South Napa, California, event, *Bull. Seismol. Soc. Am.* **107,** 1019–1026.

Infantino, M., I. Mazzieri, A. G. Özcebe, R. Paolucci, and M. Stupazzini (2021). 3D physics-based numerical simulations of ground motion in Istanbul from earthquakes along the Marmara segment of the north Anatolian fault, *Bull. Seismol. Soc. Am.* **110,** no. 6, 2559–2576, doi: 10.1785/0120190235.

Infantino, M., C. Smerzini, and J. Lin (2021). Spatial correlation of broadband ground motions from physics-based numerical simulations, *Earthq. Eng. Struct. Dynam.* doi: 10.1002/eqe.3461.

Irikura, K., and H. Miyake (2011). Recipe for predicting strong ground motion from crustal earthquake scenarios, *Pure Appl. Geophys.* **168,** 85–104.

Isbiliroglu, Y., R. Taborda, and J. Bielak (2015). Coupled soil-structure interaction effects of building clusters during earthquakes, *Earthq. Spectra* **31,** no. 1, 463–500.

Komatitsch, D., S. Tsuboi, and J. Tromp (2013). The spectral-element method in seismology, in *Seismic Earth: Array Analysis of Broadband Seismograms*, Geophysical Monograph Series 157 Copyright 2005 by the American Geophysical Union, Vol. 157, 205–227.

Lanzano, G., S. Sgobba, L. Luzi, R. Puglia, F. Pacor, C. Felicetta, M. D'Amico, F. Cotton, and D. Bindi (2018). The pan-European engineering strong motion (ESM) flat-file: Compilation criteria and data statistics, *Bull. Earthq. Eng.* **17,** 561–582, doi: 10.1007/s10518-018-0480-z.

Leonard, M. (2010). Earthquake fault scaling: Self-consistent relating of rupture length, width, average displacement, and moment release, *Bull. Seismol. Soc. Am.* **100,** no. 5A, 1971–1988, doi: 10.1785/0120090189.

Lu, X., Y. Tian, G. Wang, and D. Huang (2018). A numerical coupling scheme for nonlinear time history analysis of buildings on a regional scale considering site-city interaction effects, *Earthq. Eng. Struct. Dynam.* **47,** no. 13, 2708–2725.

Maeda, T., A. Iwaki, N. Morikawa, S. Aoi, and H. Fujiwara (2016). Seismic-hazard analysis of long-period ground motion of Megathrust earthquakes in the Nankai trough based on 3D finite-difference simulation, *Seismol. Res. Lett.* **87,** no. 6, 1265–1273, doi: 10.1785/0220160093.

Mai, P. M., and G. C. Beroza (2000). Source scaling properties from finite-fault-rupture models, *Bull Seismol. Soc. Am.* **90,** no. 3, 604–615.

Mai, P. M., and G. C. Beroza (2003). A hybrid method for calculating near-source, broadband seismograms: Application to strong motion prediction, *Phys. Earth Planet. In.* **137,** nos. 1/4, 183–199.

Maufroy, E., E. Chaljub, F. Hollender, J. Kristek, P. Moczo, P. Klin, E. Priolo, A. Iwaki, T. Iwata, V. Etienne, *et al.* (2015). Earthquake ground motion in the Mygdonian Basin, Greece: The E2VP verification and validation of 3D numerical simulation up to 4 Hz, *Bull. Seismol. Soc. Am.* **105,** no. 3, 1398–1418.

Mavroeidis, G. P., and A. S. Papageorgiou (2003). A mathematical representation of near-fault ground motions, *Bull Seismol. Soc. Am.* **93,** no. 3, 1099–1131.

Mazzieri, I., M. Stupazzini, R. Guidotti, and C. Smerzini (2013) SPEED: SPectral Elements in Elastodynamics with Discontinuous Galerkin: A non-conforming approach for 3D multi-scale problems, *Int. J. Numer. Meth. Eng.* **95,** no. 12, 991–1010.

McCallen, D. M., A. Petersson, A. Rodgers, A. Pitarka, M. Miah, F. M. Petrone, B. Sjogreen, N. Abrahamson, and H. Tang (2020). EQSIM—A multidisciplinary framework for fault-to-structure earthquake simulations on exascale computers part I: Computational models and workflow, *Earthq. Spectra*, doi: 10.1177/8755293020970982.

McCallen, D. M., F. M. Petrone, M. Miah, A. Pitarka, A. Rodgers, and N. Abrahamson (2020). EQSIM—A multidisciplinary framework for fault-to-structure earthquake simulations on exascale computers, part II: Regional simulations of building response, *Earthq. Spectra* doi: 10.1177/8755293020970980.

Norme Tecniche per le Costruzioni (NTC) (2018). *Gazzetta Ufficiale della Repubblica Italiana*, 42, 20 February 2018 (in Italian).

Özcebe, A. G., C. Smerzini, R. Paolucci, H. Pourshayegan, R. Rodríguez Plata, C. G. Lai, E. Zuccolo, F. Bozzoni, and M. Villani (2019). On the comparison of 3D, 2D, and 1D numerical approaches to predict seismic site amplification: The case of Norcia basin during the M6.5 2016 October 30 earthquake, *Proc. of the 7th International Conference on Earthquake Geotechnical Engineering*, Rome, Italy, 17–20 June.

Pacor, F., C. Felicetta, G. Lanzano, S. Sgobba, R. Puglia, M. D'Amico, E. Russo, G. Baltzopoulos, and I. Iervolino (2018). NESS1: A worldwide collection of strong-motion data to investigate near-source effects, *Seismol. Res. Lett.* **89,** no. 6, 2299–2313.

Paolucci, R., L. Evangelista, I. Mazzieri, and E. Schiappapietra (2016). The 3D numerical simulation of near-source ground motion during the Marsica earthquake, central Italy, 100 years later, *Soil Dynam. Earthq. Eng.* **91,** 39–52.

Paolucci, R., F. Gatti, M. Infantino, C. Smerzini, A. G. Özcebe, and M. Stupazzini (2018). Broadband ground motions from 3D physics-based numerical simulations using artificial neural networks, *Bull. Seismol. Soc. Am.* **108,** 1272–1286.

Paolucci, R., I. Mazzieri, G. Piunno, C. Smerzini, M. Vanini, and A. G. Özcebe (2021). Earthquake ground motion modelling of induced seismicity in the Groningen gas field, *Earthq. Eng. Struct. Dynam.* **50,** 135–154, doi: 10.1002/eqe.3367.

Paolucci, R., I. Mazzieri, and C. Smerzini (2015). Anatomy of strong ground motion: Near-source records and 3D physics-based numerical simulations of the M_w 6.0 May 29 2012 Po Plain earthquake, Italy, *Geophys. J. Int.* **203,** 2001–2020.

Paolucci, R., I. Mazzieri, C. Smerzini, and M. Stupazzini (2014). *Physics-based earthquake ground shaking scenarios in large urban areas*, in *Perspectives on European Earthquake Engineering and Seismology, Geotechnical, Geological and Earthquake Engineering*, Chapter 10, A. Ansal (Editor), Vol. 34, 331–359, doi: 10.1007/978-3-319-07118-3_10.

Pilz, M., S. Parolai, M. Stupazzini, R. Paolucci, and J. Zschau (2011). Modelling basin effects on earthquake ground motion in the Santiago de Chile basin by a spectral element code, *Geophys. J. Int.* **187,** 929–945, doi: 10.1111/j.1365-246X.2011.05183.x.

Pitarka, A., R. W. Graves, K. Irikura, K. Miyakoshi, and A. Rodgers (2020). Kinematic rupture modeling of ground motion from the M7 Kumamoto, Japan, earthquake, *Pure Appl. Geophys.* **177,** 2199–2221, doi: 10.1007/s00024-019-02220-5.

Pousse, G., L. Bonilla, F. Cotton, and L. Margerin (2006). Nonstationary stochastic simulation of strong ground motion time histories including natural variability: Application to the Knet Japanese database, *Bull. Seismol. Soc. Am.* **96,** no. 6, 2103–2117.

Rathje, E. M., N. A. Abrahamson, and J. D. Bray (1998). Simplified frequency content estimates of earthquake ground motions, *J. Geotech. Geoenviron. Eng.* **124,** no. 2, 150–159.

Sabetta, F., and A. Pugliese (1996). Estimation of response spectra and simulation of nonstationary earthquake ground motions, *Bull. Seismol. Soc. Am.* **86,** no. 2, 337–352.

Sabetta, F., A. Pugliese, G. Fiorentino, G. Lanzano, and L. Luzi (2021). Simulation of non-stationary stochastic ground motions based on recent Italian earthquakes, *Bull. Earthq. Eng.* doi: 10.1007/s10518-021-01077-1.

Sangaraju, S., R. Paolucci, and C. Smerzini (2021). 3D physics-based ground motion simulation of the 2016 Kumamoto earthquakes, *Proc. of the 6th IASPEI/IAEE International Symposium: The Effects of Surface Geology on Seismic Motion (ESG6)*, Kyoto, Japan, August 2021.

Schiappapietra, E., and C. Smerzini (2021). Spatial correlation of earthquake ground motion in Norcia (Central Italy) from broadband physics-based simulations, *Bull. Earthq. Eng.*, doi: 10.1007/s10518-021-01160-7.

Schmedes, J., R. J. Archuleta, and D. Lavallée (2012). A kinematic rupture model generator incorporating spatial interdependency of earthquake source parameters, *Geophys. J. Int.* **192,** 1116–1131.

Sgobba, S., C. Felicetta, G. Lanzano, F. Ramadan, M. D'Amico, and F. Pacor (2021). NESS2.0: An updated version of the worldwide dataset for calibrating and adjusting ground motion models in near-source, *Bull. Seismol. Soc. Am.* submitted.

Shahi, S. K., and J. W. Baker (2014). An efficient algorithm to identify strong-velocity pulses in multicomponent ground motions, *Bull. Seismol. Soc. Am.* **104,** no. 5, 2456–2466, doi: 10.1785/0120130191.

Smerzini, C. (2010). *The earthquake source in numerical modeling of seismic wave propagation in heterogeneous Earth media*, *Ph.D. Thesis*, University School for Advanced Studies in Pavia.

Smerzini, C. (2018). Spatial variability of earthquake ground motion from 3D physics-based numerical simulations, in *Proc. of the 16th European Conference on Earthquake Engineering*, Thessaloniki, Greece, 18–21 June.

Smerzini, C., and K. Pitilakis (2018). Seismic risk assessment at urban scale from 3D physics-based numerical modeling: The case of Thessaloniki, *Bull. Earthq. Eng.* **16,** no. 7, 2609–2631.

Smerzini, C., and M. Villani (2012). Broadband numerical simulations in complex near-field geological configurations: The case of the 2009 Mw 6.3 L'Aquila earthquake, *Bull. Seismol. Soc. Am.* **102,** no. 6, 2436–2451.

Smerzini, C., F. Cavalieri, S. Argyroudis, and K. Pitilakis (2018). 3D physics-based numerical modeling as a tool for seismic risk assessment of urban infrastructural systems: The case of Thessaloniki, Greece, in *Proc. of the 16th European Conference on Earthquake Engineering*, Thessaloniki, Greece, 18–21 June.

Smerzini, C., C. Galasso, I. Iervolino, and R. Paolucci (2014). Ground motion record selection based on broadband spectral compatibility, *Earthq. Spectra* **30,** no. 4, 1427–1448.

Smerzini, C., R. Paolucci, and M. Stupazzini (2011). Comparison of 3D, 2D and 1D numerical approaches to predict long period earthquake ground motion in the Gubbio plain, Central Italy, *Bull. Earthq. Eng.* **9,** no. 6, 2007–2029.

Smerzini, C., K. Pitilakis, and K. Hashemi (2017). Evaluation of earthquake ground motion and site effects in the Thessaloniki urban area by 3D finite-fault numerical simulations, *Bull. Earthq. Eng.* **15,** no. 3, 787–812.

Somerville, P. G. (2003). Magnitude scaling of the near fault rupture directivity pulse, *Phys. Earth Planet. In.* **137,** 201–212.

Somerville, P. G., N. F. Smith, R. W. Graves, and N. A. Abrahamson (1997). Modification of empirical strong ground motion attenuation relations to include the amplitude and duration effects of rupture directivity, *Seismol. Res. Lett.* **68,** no. 1, 199–222, doi: 10.1785/gssrl.68.1.199.

Stewart, J. P., S. J. Chiou, J. D. Bray, R. W. Graves, P. G. Somerville, and N. A. Abrahamson (2001). *Ground Motion Evaluation Procedures for Performance-Based Design*. PEER Report 2001/09, available at https://peer.berkeley.edu/peer-reports (last accessed July 2021).

Stupazzini, M., M. Infantino, A. Allmann, and R. Paolucci (2021). Physics-based probabilistic seismic hazard and loss assessment in large urban areas: A simplified application to Istanbul, *Earthq. Eng. Struct. Dynam.* **50,** 99–115, doi: 10.1002/eqe.3365.

Stupazzini, M., R. Paolucci, and H. Igel (2009). Near-fault earthquake ground-motion simulation in Grenoble Valley by high-performance spectral element code, *Bull. Seismol. Soc. Am.* **99,** no. 1, 286–301, doi: 10.1785/0120080274.

Taborda, R., and J. Bielak (2013). Ground-motion simulation and validation of the 2008 Chino Hills, California, earthquake, *Bull. Seismol. Soc. Am.* **103,** no. 1, 131–156

Taborda, R., and J. Bielak (2014). Ground-motion simulation and validation of the 2008 Chino Hills, California, earthquake using different velocity models, *Bull. Seismol. Soc. Am.* **104,** no. 4, 1876–1898

Thingbaijam, K. K. S., and P. M. Mai (2016). Evidence for truncated exponential probability distribution of earthquake slip, *Bull. Seismol. Soc. Am.* **106,** no. 4, 1802–1816.

Trifunac, M. D., and A. G. Brady (1975). A study on the duration of strong earthquake ground motion, *Bull. Seismol. Soc. Am.* **65,** no. 3, 581–626.

Villani, M., E. Faccioli, M. Ordaz, and M. Stupazzini (2014). High-resolution seismic hazard analysis in a complex geological configuration: The case of the Sulmona basin in Central Italy, *Earthq. Spectra* **30,** no. 4, 1801–1824.

Wells, D., and K. Coppersmith (1994). New empirical relationships among magnitude, rupture length, rupture width, rupture area, and surface displacement, *Bull. Seismol. Soc. Am.* **84,** 974–1002.

Manuscript received 22 March 2021
Published online 20 July 2021